Excitonic metal and non-Fermi liquid behavior in twisted double bilayer graphene near charge neutrality

Unmesh Ghorai [1,*] Ayan Ghosh,[2] Souvik Chakraborty,[2] Anindya Das,[2] and Rajdeep Sensarma[1]

[1]*Department of Theoretical Physics, Tata Institute of Fundamental Research, Homi Bhabha Road, Mumbai 400005, India*
[2]*Physics Department, Indian Institute of Science, Bengaluru 560012, India*

Twisted double bilayer graphene is a compensated semimetal near the charge neutrality point with the presence of small electron and hole pockets in its band structure. We show that strong Coulomb attraction between the electrons and holes can lead to the formation of indirect excitons. Condensation of these excitons at low temperature creates an excitonic metal with charge density wave order for an appropriate range of interaction strength. This has interesting implications for low-temperature transport in the system as a function of carrier density and temperature. The reorganization of the single-particle excitations and their density of states in the excitonic metal can lead to peaks in resistivity as a function of carrier density, recently seen in experiments at low temperatures. The fluctuations of the Landau damped order parameter in the quantum critical metal lead to non-Fermi liquid behavior, which can explain the sublinear $T^{2/3}$ dependence of the resistance near the charge neutrality point.

I. INTRODUCTION

When sheets of two-dimensional materials are stacked on top of each other and their crystal axes are twisted (rotated) by a small angle, the electronic structure of these heterostructures becomes extremely sensitive to the angle of twist between them [1–10]. This has led to the idea of twistronics [6,11], where the twist angle will be used as an experimental knob to change the electronic properties of these systems. The tunability of electronic structure with twist angles has been successfully studied in a controlled fashion in several systems, including multiple layers of graphene [11–16] and Bernal stacked bilayer graphene [17–19], graphene-boron nitride sandwiches [20], and heterostructures made of dichalcogenides [21,22]. A common feature of these systems is the presence of (multiple) magic twist angles [1,7], where the bandwidth of the system is a minimum and the fate of the system is determined by strong electronic interactions. In graphene-based systems, such magic angles occur around 1–1.6 ° [14,23,24], leading to large incommensurate moiré unit cells ∼8–15 nm.

In twisted bilayer graphene (tBLG), where two sheets of graphene are twisted with respect to each other, the electronic interactions lead to a plethora of symmetry-broken phases as a function of the electron density at the magic angle, from correlated insulators [11,23,25] to orbital ferromagnets [26] to superconductors [12,13,23,27,28]. In twisted trilayer graphene (tTLG), where three sheets of graphene are twisted with respect to each other, the electronic correlations again lead to a superconducting state over a range of carrier densities [14,15,29,30]. In comparison, their close cousin, the twisted double bilayer graphene (tDBLG), where two sheets of Bernal stacked bilayer graphene are rotated with respect to each other, had shown a simple metallic behavior as a function of

filling in early experiments [17,19]. While there is evidence of correlated behavior in the presence of perpendicular electric [17,18,24,31] or magnetic [17,31] fields, the phenomenology of tDBLG in the absence of these fields can be explained by a noninteracting picture [9,10,17,19].

The metallic behavior of tDBLG even near the charge neutrality point (CNP) with no external doping is readily explained by the fact that the flat valence and conduction bands in tDBLG overlap with each other in energy. This leads to the formation of small electron and hole pockets in this regime [9,10,32]. tDBLG at the CNP is thus a compensated semimetal. The presence of these electron and hole pockets near the CNP in tDBLG has now been demonstrated unambiguously through recent magnetotransport measurements [33]. This brings us to an interesting question: Do the strong electronic interactions have any qualitative effect on the small electron and hole pockets near the CNP or do they behave like almost noninteracting systems? In this paper, we show that indirect excitons are formed due to the attraction between the electron and hole pockets, and condensation of these excitons can lead to the formation of a charge density wave (CDW) state near the CNP at low temperatures. The system remains metallic on either side of the transition for a range of parameters. The phase transition in the background of itinerant electrons is driven by Landau damped fluctuations of the excitonic order. The scattering of electrons by these fluctuations leads to non-Fermi liquid behavior in these systems [34–42]. Thus interactions have profound effects on the small electron and hole pockets in the system. In this context, we would like to note that there are several theoretical works [43–47] which propose a particle-hole asymmetric band structure even for tBLG and tTLG with the possible formation of e-h pockets near the CNP. These electrons and holes can also form excitonic bound states. However, in tBLG and tTLG, the experiments [11,13–15,23,26] show insulating behavior near the CNP. Therefore, even if excitons are formed, they are likely to form insulating states in these systems.

*unmesh.ghorai@tifr.res.in

The formation of an excitonic condensate leads to a reorganization of the electronic structure into multiple "minibands" with their respective Fermi seas. This leads to anomalous peaks in the inverse density of states at the Fermi level as a function of carrier density, which mimics the peaks in resistance as a function of carrier density seen in recent experiments [33]. Within a mean-field theory, the simultaneous presence of the anomalous peaks as well as a Fermi sea to account for metallic behavior strongly constrains the interaction parameters. We find that the allowed parameter ranges are reasonable for tDBLG.

Another surprising result from these experiments [33] is that close to the CNP, the measured resistance exhibits a unique sublinear temperature dependence ($R \sim T^{2/3}$) in the temperature range 0–10 K. Above this temperature range, the resistance increases linearly with temperature. Far away from the CNP, the resistance reverts to a standard superlinear temperature dependence ($R \sim T^2$) seen in usual metals. The sublinear temperature dependence of resistivity is rarely seen in metals and cannot be explained by standard scattering mechanisms (disorder, electron-electron, or electron-phonon) within a Fermi liquid theory. On the other hand, in a quantum critical metal on the verge of forming excitonic condensates, the quantum fluctuations of the order parameter will be Landau damped by the low-energy fermions present in the system. We show that the scattering of charge carriers in the small Fermi pockets from such overdamped critical fluctuations gives rise to a non-Fermi liquid with a $T^{2/3}$ dependence of resistance at low temperatures. At higher temperatures, we reach an equivalent of a "Bloch Gruneissen" temperature for these fluctuations and the resistivity shows linear temperature dependence beyond that scale. The question of a breakdown of Fermi liquid theory in a metal due to quantum fluctuations near a critical point is a matter of great theoretical interest and has been studied using sophisticated formalisms [34,37–42]. Here we propose that the presence of small Fermi surfaces in these systems undergoing phase transitions ensures that the non-Fermi liquid behavior shows up in low-temperature transport as a nonanalytic temperature dependence of the resistivity. Thus we propose that the magic angle tDBLG is not a garden-variety metal; rather, there is strong experimental evidence for an underlying non-Fermi liquid state formed due to interactions in a compensated semimetal.

In this paper, we review the formation of electron and hole pockets in tDBLG in Sec. II. Section III provides the details of the mean-field theory of the excitonic condensate near the CNP. In Sec. IV, we show how the electronic reorganization due to exciton formation leads to peaks in the inverse density of states and compare it to experiments. In Sec. V, we discuss how the Landau damping near a critical point leads to a non-Fermi liquid behavior. We also discuss the connection of this underlying non-Fermi liquid state to the sublinear temperature dependence in resistivity. Finally, in Sec. VI, we conclude with a summary of our results.

II. ELECTRON AND HOLE POCKETS IN tDBLG

The low-energy electronic states of tDBLG at magic angle at and around the CNP consist of both electron and hole pockets. This is in contrast to other members of the twisted
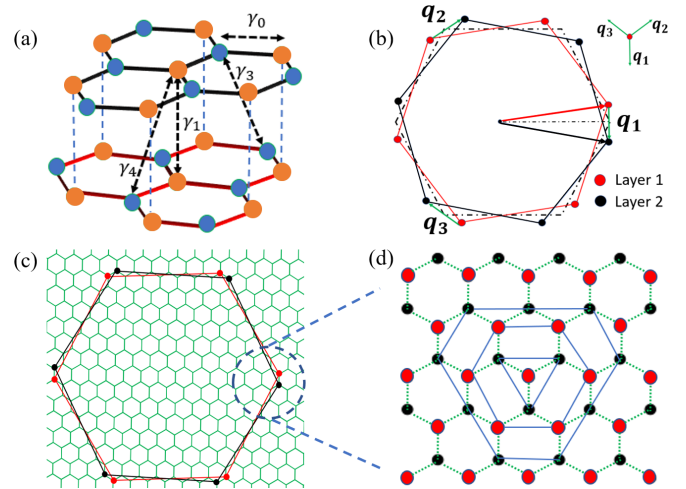

FIG. 1. (a) Schematic of Bernal stacked bilayer graphene and relevant intralayer (γ_0) and interlayer ($\gamma_{1(3)(4)}$) tunnelings. (b) Brillouin zone of two bilayer graphene sheets rotated with respect to each other by a small twist angle. Three transfer momenta ($q_{1(2)(3)}$) between the Dirac points of each layer are marked. (c), (d) The smaller moiré Brillouin zone created by the twist. The zoomed-in image shows the construction of consecutive shells and the momentum cutoff used in the continuum model.

graphene family (tBLG or tTLG), which form a Dirac node at the CNP and show either electron- or holelike states when doped away from the CNP [1,3,10,32,48,49]. As a result, tDBLG shows metallic behavior near the CNP, while the other moiré graphene systems show weakly insulating ($R \sim 10$–50 kΩ) behavior [11,13–15,19,24,29,50]. There are a number of theoretical works [43–47] which propose a particle-hole asymmetric band structure even for tBLG and tTLG with the possible formation of electron-hole (e-h) pockets near the CNP. In this case, one would again expect the formation of excitons due to the attraction of electrons and holes. Experimental evidence [11,13–15,23,26] shows insulating behavior near the CNP in these materials, which indicates that these states are gapped out. The gap could be either due to the formation of an excitonic insulator or the breaking of other symmetries.

Since tDBLG is made of two layers of bilayer graphene (BLG) with a twist between them, it is useful to start with the band structure of BLG. A schematic of a Bernal (A-B) stacked BLG is shown in Fig. 1(a). The carbon atoms in each layer form a honeycomb lattice and are coupled by a nearest-neighbor in-plane hopping γ_0, where $\frac{\sqrt{3}}{2}\gamma_0 = \hbar v_0/a \sim 2.1354$ eV [32], while the out-of-plane hopping is primarily between atoms which sit on top of each other (in the so-called dimer sites) with a scale $\gamma_1 = 400$ meV. A simplified model of BLG with only γ_0 and γ_1 produces a Dirac point where two quadratic bands touch each other, with a Berry monopole of charge 2 located at the Dirac point. However, if one considers additional interlayer hoppings between the nondimerized sites (the trigonal warping $\gamma_3 = 320$ meV), or between dimerized and nondimerized sites ($\gamma_4 = 44$ meV), this simple picture changes at low energies. The single band touching point splits into a central Dirac point and three satellite Dirac points, where linearly dispersing bands touch
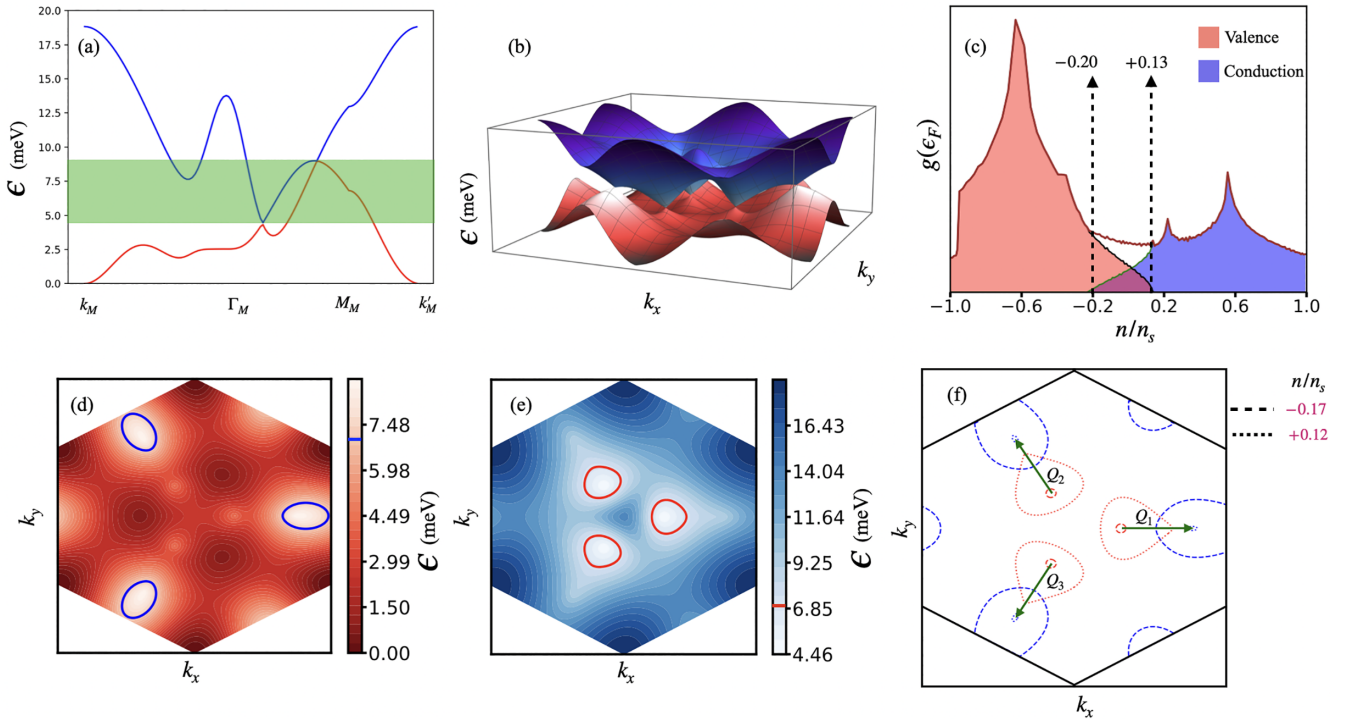
FIG. 2. (a) Noninteracting band dispersion of tDBLG along high-symmetry directions in the moiré Brillouin zone. The valence (red) and conduction (blue) bands are plotted. The shaded region denotes the energies where the bands overlap. (b) A 3D depiction of the energy dispersion in the mBZ to show the six satellite Dirac points around the Γ_M point. (c) Valence (red) and conduction (blue) bands' density of states at the Fermi level are plotted with the normalized carrier density. The bands overlap between carrier densities (marked) ≈ -0.20 and 0.13. (d), (e) Contour plots of the valence (red) and conduction (blue) bands, respectively, with Fermi surfaces at the CNP marked separately. The blue pocket in (d) and the red pocket in (e) denote the hole and electron pocket, respectively. (f) The electron (red) and hole (blue) pockets at two different carrier densities around the CNP are shown to point out that one of the pockets shrinks and another one inflates as one moves away from the CNP. The $Q_{1(2)(3)}$ vectors connect the e-h pocket centers and are related by C_3 symmetry.

each other [51]. The central and the satellite Dirac points carry Berry monopoles of opposite charges. The formation of the satellite Dirac points and associated Lifshitz transitions in BLG have been probed both theoretically and experimentally [52,53]. We also include an on-site potential of dimerized sites with respect to nondimerized sites, $\delta' = 50$ meV [32].

We consider the AB-AB stacked tDBLG. In this case, the graphene Brillouin zone is tiled by the moiré Brillouin zone (mBZ), with a reciprocal lattice vector of size $k_M = k_D \sin\theta/2$, where k_D is the reciprocal lattice vector of the BLG Brillouin zone and θ is the twist angle, as shown in Fig. 1(b). The two twisted layers are tunnel coupled with tunneling between the same sublattices, $u_{AA} = u_{BB} = 79.7$ meV, and the tunneling between different sublattices, $u_{AB} = 97.5$ meV. For these sets of parameters, used in a wide range of earlier papers [10,24,32], the magic angle is 1.2°, which matches with experimental estimates of the magic angle for tDBLG [33]. The inter-BLG tunnelings couple momentum states in one mBZ to those in nearby zones, as shown in Ref. [1] and Figs. 1(c) and 1(d). One can limit the number of Brillouin zones used to calculate the band dispersion of the moiré system at low twist angles [1]. We use the five nearest shells, which lead to a 184-dimensional continuum Hamiltonian to obtain the low-energy band dispersion of tDBLG within an accuracy of 1%.

The low-energy band structure of tDBLG near the magic angle consists of a valence and a conduction band with a

bandwidth ∼20 meV. In Fig. 2(a), we plot the dispersion of the conduction and valence bands along the principal directions of the mBZ ($K_M - \Gamma_M - M_M - K'_M$). We clearly see that the bands overlap in energy along the $\Gamma_M - M_M$ line [shown by the shaded region in Fig. 2(a)]; hence, at the charge neutrality point, one would expect a compensated metal with electron and hole pockets. We would like to note that particle-hole symmetric band structures, obtained from a simplified description of BLG with only γ_0 and γ_1, do not show this band overlap [9,10]. The presence of trigonal warping γ_3 is crucial in obtaining this overlap. In Fig. 2(b), we show a three-dimensional (3D) plot of the dispersion of the valence and the conduction bands, which clearly shows that the bands do not cross each other; rather, they touch each other at two anisotropic Dirac points along the $\Gamma - M$ line at slightly different energies, leading to the band overlap. The valence and conduction band dispersions are plotted as color plots in the full Brillouin zone in Figs. 2(d) and 2(e). The thick lines mark the Fermi surfaces (curves) of the electron (conduction band) and hole (valence band) pockets at the CNP. We clearly see that there are three electron and three hole pockets related by C_3 symmetry. The pockets are centered around the points where the bands touch each other. We note that we have plotted the moiré bands around one valley of the original BLG dispersion. The band touchings and electron-hole pockets of the other valley can be obtained by applying a rotation of π to this figure. As we move away from the CNP on the

electron-doped side, the size of the electron pocket increases, while the hole pocket shrinks. At an electron density $n/n_s \sim 0.13$, the hole pocket shrinks to a point and beyond this density the system only has three electron pockets. Here, $n_s \approx 3.3 \times 10^{12}$ cm^{-2} is the density where the conduction band is fully filled (including spin and valley degeneracies). On the other hand, with hole doping, the hole pocket grows and the electron pocket shrinks, until it disappears at $n/n_s \sim -0.2$. Figure 2(f) plots the Fermi surfaces for the electron and hole pockets on either side of the CNP at densities $n/n_s = -0.17$ and $n/n_s = 0.12$ to show the evolution described above. Note that the centers of the pockets do not change with density and the wave vectors joining the centers of the nearest electron and hole pockets, $\mathbf{Q}_1$, $\mathbf{Q}_2$, and $\mathbf{Q}_3$, are clearly shown in Fig. 2(f). While there is an interesting evolution of the Fermi surface at higher densities, in this paper, we will focus on densities between $n/n_s = -0.2$ and $n/n_s = 0.13$, where both electron and hole pockets are present.

The finite density of states at the Fermi level coming from these electron and hole pockets lead to metallic behavior in tDBLG [17–19,24,50] in the absence of a perpendicular electric field. We note that the waxing and waning of the electron and hole pockets compensate each other to keep the total density of states at the Fermi level finite and independent of the carrier density near the CNP, as shown in Fig. 2(c). Recently, the strong magnetic field dependence of the low-temperature resistance and thermopower in these systems [33] have provided concrete evidence of the existence of these electron and hole pockets in tDBLG.

In our model, we have checked that for a twist angle range of 1.1 to 1.7 degrees, the e-h pockets can be present.

We note that some calculations [54–56] predict a gap in the spectrum of tDBLG in the presence of a crystal field, in which case our description will not work. However, there is strong experimental evidence [17,19,24,50] for metallic behavior at the CNP for tDBLG which is contradictory to the large gap predicted by these calculations.

III. EXCITON CONDENSATES NEAR CNP

An important question in systems with low electronic density is the following: What is the fate of the system when the strong electronic interactions are taken into account? While earlier experiments in tDBLG [17–19,24,50] showed a fairly standard metallic behavior in the absence of perpendicular electric fields (correlated states were found at finite electric fields), a recent experiment [33] at very low temperatures ($T < 2$ K) has shown a double-peak structure in the resistance as a function of carrier density near the CNP where both electron and hole pockets are present. These double-peak structures cannot be explained by a noninteracting theory since electrons and holes contribute additively to the electrical response, and the total density of states near the CNP is almost independent of doping, as seen in Fig. 2(c). These are concrete experimental signatures that electronic correlations play an important role in tDBLG near the CNP.

In systems with electron and hole states at the Fermi level, the Coulomb attraction between the oppositely charged electrons and holes often leads to the formation of charge neutral electron-hole pairs called excitons. The formation of

exciton states is commonly seen in semiconductor systems [57,58], as well as van der Waals heterostructures [59,60]. Coherent condensation of these particle-hole pairs, leading to superfluidity of charge neutral objects, has been predicted and demonstrated in bilayer quantum Hall systems [61–64], as well as bilayer graphene [65]. The electron-hole pockets in tDBLG, which are separated by a small momentum $|\mathbf{Q}_i| \sim 0.01$ Å^{-1}, are ideal candidates for the formation of excitonic condensates with finite momentum (indirect excitons). We will now explore this possibility within mean-field theory.

We consider the two-band Hamiltonian,

$$H = \sum_{\mathbf{k}\eta} \left(\epsilon_{\mathbf{k}}^c - \mu\right) C_{\mathbf{k},\eta}^{c\dagger} C_{\mathbf{k},\eta}^c + \left(\epsilon_{\mathbf{k}}^v - \mu\right) C_{\mathbf{k},\eta}^{v\dagger} C_{\mathbf{k},\eta}^v$$
$$+ \frac{1}{\Omega} \sum_{\mathbf{k},\mathbf{k}',\mathbf{q},\eta\eta'} V(\mathbf{q}) C_{\mathbf{k}+\mathbf{q},\eta}^{v\dagger} C_{\mathbf{k},\eta}^v C_{\mathbf{k}'-\mathbf{q},\eta'}^{c\dagger} C_{\mathbf{k}',\eta'}^c, \quad (1)$$

where $C^{c(v)}$ denotes the electron annihilation operator in the conduction (valence) band, η is a composite spin and valley index, and $\epsilon_{\mathbf{k}}^{c(v)}$ is the conduction and valence band dispersions shown in the previous section. Here, $V(\mathbf{q})$ is the screened Coulomb interaction between the conduction and valence band electrons. We note that we have neglected repulsive interaction between electrons in the same band since our primary focus is on understanding the formation of interband excitons. We note that in contrast to tBLG, where the normal state band structure is strongly renormalized by repulsive interaction in a doping-dependent manner [66–68], the band structure in tDBLG is robust to such interaction effects [69]. This allows us to neglect repulsive intraband interactions. Since the interaction scales are comparable to Fermi energy, one can also worry whether the repulsive interaction can lead to alternate symmetry-broken states. Note that there is no nesting of Fermi surfaces in the problem. Hence, one expects the attractive BCS-type interaction (which we have kept) to be the leading instability, in contrast to the repulsive interaction which we have left out. We have also assumed that the large momentum connecting the two valleys of BLG, ~ 1 Å^{-1}, makes it unfavorable for Coulomb interaction to scatter electrons from one valley to the other. Note that although excitons are often understood as the pairing of electrons and holes, where the hole can be obtained by a particle-hole transformation on the valence band, i.e., $C^v \to h^{v\dagger}$, we prefer to work with electron coordinates in both bands. The size of the small Fermi pockets as well as the momentum separating the center of the electron and hole pockets are ~ 0.01 Å^{-1}. We assume that $V(\mathbf{q})$ does not change rapidly over this scale and can be approximated by a constant value V_0 for our calculation. Note that the extended Kang-Vafek-like terms vanish in the absence of flat band topology in this system [70]. For our calculations, we will use $u_0 = 10.9$ meV, where $u_0 = V_0/\Omega$. We will later try to constrain its value both from theoretical and experimental estimates. If we denote the density of states per electron pocket by χ, this gives $V_0\chi \sim 0.2$. If we assume the intraband interaction has a similar magnitude, we are far away from any possible Stoner instability, which further justifies the omitting of intraband interaction in our model.

From Fig. 2(f), we see that there are three electron and hole pockets in the mBZ, and three wave vectors $\mathbf{Q}_{1(2)(3)}$
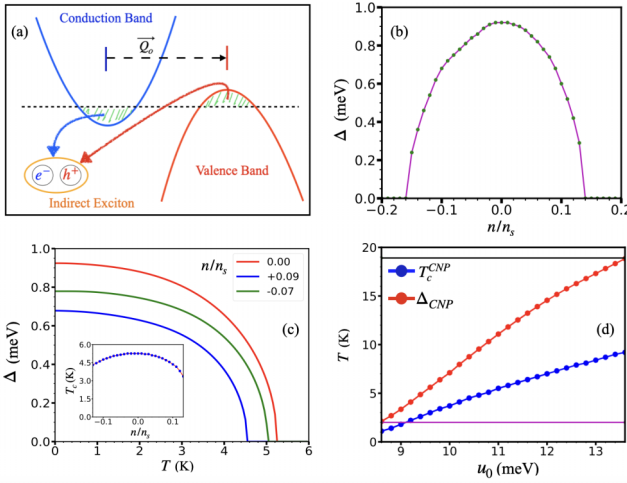
FIG. 3. (a) Schematic showing the formation of indirect excitons from the two bands. (b) Mean field order parameter (Δ) plotted with carrier density. Δ has a peak at the CNP and goes down on either side of the CNP. (c) The temperature dependence of Δ is shown for three values of $n/n_s = 0.00, 0.09, -0.07$. Inset: The variation of T_c with density around the CNP. T_c is weakly dependent on n/n_s, with a peak at the CNP. (d) Δ (in units of temperature) (red) and mean field T_c (blue) plotted as a function of the interaction strength u_0. The pink line is the experimentally observed T_c. The black line indicates Δ_c, where the system forms an excitonic insulator rather than a metal for $\Delta > \Delta_c$.

connecting them. We will consider a mean-field description of the finite momentum interband excitonic condensate, which has an equal amplitude at each of the momenta $\mathbf{Q}_i$, i.e., $\frac{V_0}{\Omega}\sum_{\mathbf{k}}\langle C_{\mathbf{k},\eta}^{\dagger c} C_{\mathbf{k}+\mathbf{Q}_i,\eta}^v\rangle = \Delta$ [see Fig. 3(a) for a schematic of the finite momentum exciton]. We note that the formation of finite momentum excitonic condensates in this system is equivalent to the appearance of a charge density wave (CDW) order in the system. Since $\sum_i \mathbf{Q}_i = 0$, our ansatz of equal condensates for all momenta ensures that there is no underlying valley current in the ground state of the system. It also ensures that the C_3 symmetry of each valley remains unbroken in the system. Further, in Appendix C, we discuss within a Landau-Ginzburg theory why the equal amplitude order is likely to be the lowest-energy state. Note that $\mathbf{Q}_i \rightarrow -\mathbf{Q}_i$, if the valley is flipped, and the net current summed over valleys would have been zero even for an ansatz with unequal condensates. With this ansatz, using the basis $(C_{\mathbf{k}}^c, C_{\mathbf{k}+\mathbf{Q}_1}^v, C_{\mathbf{k}'}^c, C_{\mathbf{k}'+\mathbf{Q}_2}^v, C_{\mathbf{k}''}^c, C_{\mathbf{k}''+\mathbf{Q}_3}^v)$, we obtain the 6×6 mean-field Hamiltonian,

$$\mathcal{H} = \begin{bmatrix} d_{\mathbf{Q}_1}(\mathbf{k}) & 0 & 0 \\ 0 & d_{\mathbf{Q}_2}(\mathbf{k}') & 0 \\ 0 & 0 & d_{\mathbf{Q}_3}(\mathbf{k}'') \end{bmatrix}, \quad (2)$$

where

$$d_{\mathbf{Q}_i}(k) = \begin{bmatrix} \frac{\epsilon_{\mathbf{k}}^c}{3} - \mu & \Delta \\ \Delta & \frac{\epsilon_{\mathbf{k}+\mathbf{Q}_i}^v}{3} - \mu \end{bmatrix}. \quad (3)$$

Here, $\mathbf{k}'$ and $\mathbf{k}''$ vectors are generated by rotating the $\mathbf{k}$ vector by $2\pi/3$ and $4\pi/3$, respectively. The quasiparticle excitation

spectrum of the mean-field theory is

$$E_{\mathbf{Q}_i}^{\pm}(\mathbf{k}) = \frac{\epsilon_{\mathbf{k}}^c + \epsilon_{\mathbf{k}+\mathbf{Q}_i}^v}{6} - \mu \pm \sqrt{\frac{\left(\epsilon_{\mathbf{k}}^c - \epsilon_{\mathbf{k}+\mathbf{Q}_i}^v\right)^2}{36} + \Delta^2}. \quad (4)$$

The self-consistency equations, which determine the order parameter Δ and the chemical potential μ, are given by

$$1 = \frac{V_0}{2\,\Omega}\sum_{\mathbf{k},\mathbf{Q}_i}\frac{-1}{E_{\mathbf{k}}^{\mathbf{Q}_i}}[f(E_{\mathbf{Q}_i}^+(\mathbf{k})) - f(E_{\mathbf{Q}_i}^-(\mathbf{k}))],$$

$$n = \frac{1}{3}\sum_{\mathbf{k},\mathbf{Q}_i}[f(E_{\mathbf{Q}_i}^+(\mathbf{k})) + f(E_{\mathbf{Q}_i}^-(\mathbf{k}))], \quad (5)$$

where f is the Fermi function. Here, $E_{\mathbf{k}}^{\mathbf{Q}_i}$ is defined as, $[\sqrt{(\epsilon_{\mathbf{k}}^c - \epsilon_{\mathbf{k}+\mathbf{Q}_i}^v)^2/36 + \Delta^2}]$. In Fig. 3(b), we plot the self-consistent Δ at $T = 0$ as a function of the carrier density n/n_s for a system with $u_0 = 10.9$ meV. The order parameter shows a maxima around the CNP (~ 0.9 meV) and decreases on either side of the CNP, finally vanishing through a sharp jump at the boundaries where the electron-hole pockets cease to exist simultaneously. The electron and hole pockets are matched in size (albeit shifted in momentum) at the CNP. As we move away, the electron (hole) pocket grows, while the hole (electron) pocket shrinks. This mismatch of the Fermi pockets leads to a weakening of the order parameter at finite carrier densities. The temperature dependence of the order parameter at three different densities is shown in Fig. 3(c). From the vanishing of the order parameter, one can obtain the mean-field T_c of the system, which is plotted in the Fig. 3(c) inset as a function of carrier density. We see that T_c is very weakly dependent on carrier density and hovers around 5 K for our chosen set of parameters. Our estimate is in the same ballpark as the experimentally obtained $T_C \sim 2$ K [33], where the resistance peaks disappear. We would like to note that this mean-field estimate is an upper bound for the real T_c, which will be further degraded by fluctuations and disorder. In Fig. 3(d), we have shown the u_0 dependence of $\Delta(T = 0)$ and T_c at the CNP. The magenta horizontal line is the experimentally observed $T_c \sim 2$ K [33]. The black horizontal line corresponds to the maximum value of $\Delta(T = 0)$ for which the system remains metallic (see discussion in Sec. IV for details). These two lines thus provide lower and upper bounds on u_0 (9.1 meV and 13.6 meV, respectively) to be used in the calculation. We have used $u_0 = 10.9$ meV in the middle of this range.

IV. EXCITON CONDENSATES AND ELECTRONIC STRUCTURE

The occurrence of exciton condensates in materials [57–59,71] often leads to the underlying Fermi surface being gapped out, leading to an excitonic insulator. This is inevitably the case when the condensate is formed with zero net momentum, as is the case in quantum Hall bilayers and bilayer graphene [61–65]. However, the shift between the center of the electron and hole pockets in tDBLG near the CNP naturally leads to excitonic condensates with finite momenta. This leads to the possibility of having either metallic or insulating behavior depending on the magnitude of the
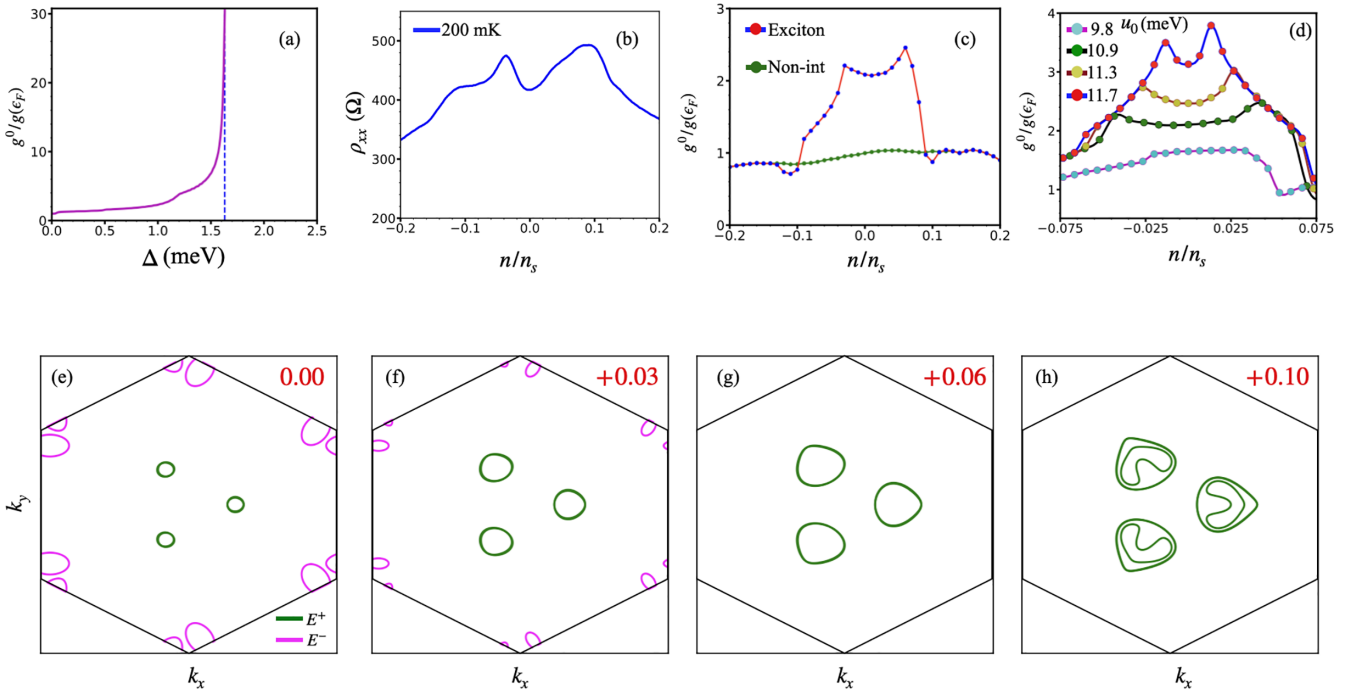
FIG. 4. (a) Inverse DOS at the Fermi energy for the excitonic metal is plotted with Δ. For $\Delta > \Delta_c \sim 1.6$ meV (marked by the blue dotted line), the system shows insulating behavior with zero density of states at the Fermi level. (b) Experimentally obtained longitudinal resistivity of tDBLG as a function of carrier density at 200 mK exhibiting the double-peak structure. (c) Inverse DOS at the Fermi level for the excitonic metal (red) and the noninteracting state (brown) as a function of carrier density. The excitonic condensate leads to two peaks in the inverse DOS similar to the experimental data in (b), whereas the noninteracting DOS at the Fermi level is almost independent of density in this regime. (d) Inverse DOS at the Fermi level of the excitonic metal for different interaction strengths plotted as a function of carrier density. The fact that the two-peak structure disappears at low interaction strength, while the system is insulating at large interaction strength, allows a small range of the interaction parameter which is compatible with the existing experimental data. We will use $u_0 = 10.9$ meV for our calculations, unless otherwise stated. (e)–(h) The evolution of the Fermi surfaces of the two exciton bands ($E^{+(-)}$) [green (pink)] in the mBZ with changing densities. For $0 < n/n_s < +0.06$, the green contours increase while the pink contours shrink. This leads to an increase in the resistivity. At $n/n_s = 0.10$, the Fermi level enters a higher miniband of the excitonic state. The additional density of states leads to a decrease in the resistivity, thus giving rise to the peak as a function of density. A similar story plays out on the other side of the CNP, leading to the double-peak structure in resistivity.

excitonic order in the system and the resulting quasiparticle spectrum $E_{\mathbf{Q}_i}^{\pm}$. Note that the original two-band system is mapped to a six-band system in the presence of excitonic order.

A simple measure of metallicity of the system is the density of states at the Fermi level, $g(\epsilon_F) = \sum_{\pm,i,\mathbf{k}} \delta[E_{\mathbf{Q}_i}^{\pm}(\mathbf{k}) - \epsilon_F]$. For metals, we expect $g(\epsilon_F)$ to be finite, while it should go to zero for insulators. We now consider how $g(\epsilon_F)$ behaves with carrier density for different values of Δ. These Δ values are not obtained from a self-consistent solution of the gap equation; rather, our intention is to vary Δ and understand the range of values for which we can recover the metallic behavior seen in the experiments. For each Δ, we solve the number equation to obtain the Fermi level for the excitonic quasiparticles. In Fig. 4(a), we plot $g^0/g(\epsilon_F)$ as a function of the order parameter Δ at the CNP. Here, g^0 is the density of states at the Fermi level of the noninteracting system at the CNP. For $\Delta > 1.63$ meV, the system is insulating in nature and below that it is a metal. Since the experimental data [33] clearly show metallic behavior at low temperatures for all densities near the CNP, this provides an upper bound for the possible values of Δ. Within the mean-field theory, this in turn provides an upper bound on the interaction strength u_0. For

$\Delta_{\mathrm{CNP}} < 1.63$ meV, we obtain $u_0 < 13.6$ meV. In this work, we use a value of $u_0 = 10.9$ meV, which is consistent with earlier work [72].

In recent experiments, the resistance of tDBLG at low temperatures has shown a distinct two-peak structure as a function of carrier density near the CNP. This is seen in the region where electron and hole pockets are simultaneously present. Representative experimental data are shown in Fig. 4(b). We will use the inverse of the density of states (DOS) at the Fermi level as a proxy for the resistivity of the system. This assumes that Fermi velocity is not sharply anisotropic in the density range considered, which is valid for tDBLG near the CNP with its small electron and hole pockets. In Fig. 4(c), we plot $g^{-1}(\epsilon_F)$ as a function of carrier density for a system with indirect excitonic condensate ($u_0 = 10.9$ meV). We clearly see the presence of two peaks, as seen in the experiments. For comparison, we have also plotted $g^{-1}(\epsilon_F)$ for the noninteracting system, which does not show any structure in the relevant density range. This shows that the presence of excitonic condensate can explain the double-peak structure seen in experiments. In Fig. 4(d), we plot $g^{-1}(\epsilon_F)$ with carrier density for different interaction strengths and see that the two-peak feature is lost for $u_0 < 10$ meV. This is close to the lower
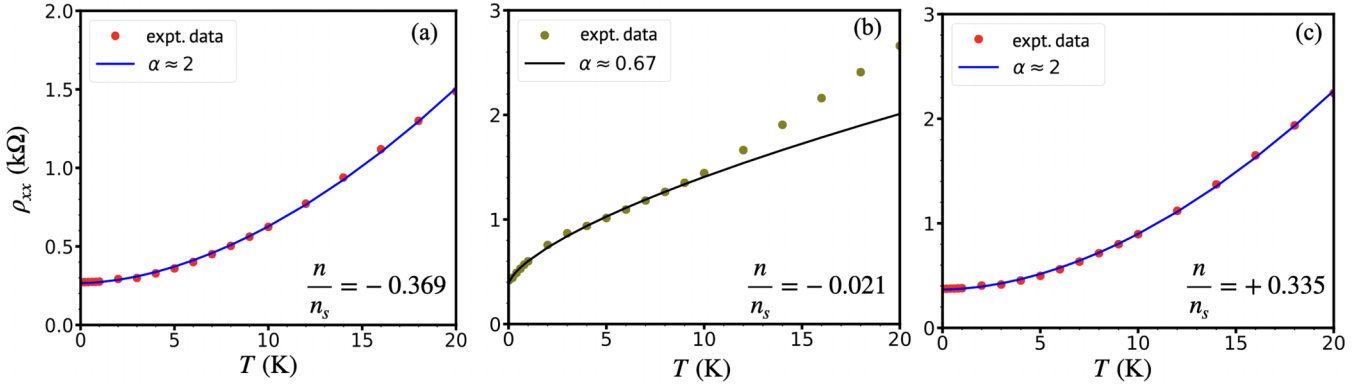
FIG. 5. The experimental data for the temperature dependence of longitudinal resistivity near and away from the CNP. Note that the noninteracting Fermi temperature $T_F \sim 23$ K. In (a) and (c), a fit to the data of the form $R_0 + A\, T^\alpha$ gives $\alpha \sim 2$, showing Fermi liquid scaling. The data near the CNP in (b) clearly show sublinear behavior of the resistivity below 10 K and an almost linear behavior above it. Here the data up to 10 K are fitted to $R_0 + A\, T^\alpha$, yielding $\alpha = 0.67$. This sublinear temperature dependence is a manifestation of an underlying non-Fermi liquid in the system.

bound obtained from experimental T_c discussed in the earlier section.

In order to theoretically understand the origin of the two peaks, we look at the dispersion of the six bands in the presence of the excitonic condensate (the detailed band dispersion of all six bands is plotted in Appendix B). In Figs. 4(e)–4(h), we plot the Fermi surfaces of the quasiparticles [with spectrum $E_{\mathbf{Q}_i}^{\pm}(\mathbf{k})$] in the mBZ for four different carrier densities, $n/n_s = 0$, 0.03, 0.06, 0.10. At the CNP [Fig. 4(e)], we find that both E^+ and E^- bands pass through the Fermi level, and hence give rise to their respective Fermi surfaces (shown by green and pink lines, respectively). This leads to the finite density of states at the Fermi energy and hence to metallic behavior in the system. As we move away from the CNP on the electron-doped side, the Fermi surfaces corresponding to E^- reduce, while those of E^+ bands increases in size [Figs. 4(e)–4(h)]. This leads to a reduction in the density of states at the Fermi level and hence to an increase in resistivity until the E^- Fermi surface vanishes at $n/n_s = 0.06$ [Fig. 4(g)], which corresponds to the peak in the inverse density of states. Beyond this point, we see additional Fermi surfaces as the chemical potential enters one of the bands which was gapped at the CNP. This leads to a large increase in the density of states at the Fermi level and consequently a sharp decrease in the resistivity, explaining the peak seen in the resistivity for $n > 0$. A similar argument, with the roles of E^+ and E^- reversed, explains the peak for $n < 0$. We would like to note that the transport features are expected to be more smeared than single-particle features due to the presence of inhomogeneities in the system. This is consistent with the experiments, which see relatively smoother features compared to the theoretical estimates.

V. TEMPERATURE DEPENDENCE OF RESISTIVITY AND NON-FERMI LIQUID BEHAVIOR

An intriguing signature of strong electronic correlations is seen in recent experiments [33] on the temperature dependence of the resistance of tDBLG near the charge neutrality point. The resistance shows a sublinear ($R = R_0 + A\, T^\alpha$ with

$\alpha \approx 2/3$) behavior up to $T \sim 10$ K, and an almost linear behavior above that temperature [Fig. 5(b)]. In contrast, the temperature dependence of resistance at larger electron (hole) densities, $n/n_s = +0.335$ and $n/n_s = -0.369$, are superlinear and can be fitted to the standard quadratic Fermi liquid scaling, $R = R_0 + A\, T^\alpha$ with $\alpha \approx 2$, expected for a 2D system with small Fermi pockets, both from electron-electron and electron-phonon scattering. This is shown in Figs. 5(a) and 5(c).

This sublinear behavior cannot be explained within a Fermi liquid paradigm of perturbative effects of electronic interactions around a free Fermi gas. Electron-electron interactions lead to a $\sim T^2$ dependence of the resistivity. In two dimensions, the density of states of longitudinal phonons $\rho(\omega) \sim \omega$. This leads to $\sim T^4$ dependence of resistivity when small angle scattering dominates at low temperatures and $\sim T^2$ behavior of resistivity when scattering at all angles contributes. For compensated semimetals such as tDBLG, with small Fermi surfaces, one would expect the resistivity $\sim T^2$. At higher temperatures (beyond the Bloch Gruneissen temperature), the scattering from classical phonons would lead to a linear T dependence of resistivity [73]. None of these mechanisms can explain a sublinear temperature dependence of resistivity, as is seen in the experiments.

In this section, we will show that a tDBLG system near the CNP, which is at the precipice of a quantum criticality towards the formation of an excitonic condensate, will show a sublinear $T^{2/3}$ temperature dependence of resistance. At criticality, the low-energy gapless fluctuations of the excitonic (CDW) order parameter would be strongly Landau damped due to the presence of the electronic states of the metal around the Fermi surfaces. The scattering between electrons and the Landau damped fluctuations leads to a nonanalytic low-energy decay rate for the single-particle electronic excitations, resulting in non-Fermi liquid behavior. For compensated semimetals such as tDBLG, with small Fermi surfaces, the transport scattering rate and the quasiparticle scattering rate have the same energy dependence. This nonanalytic frequency dependence of the scattering rate leads to the sublinear temperature dependence of resistivity in this system. We note that this mechanism is an

alternate to theories of Planckian metal [74], which predicts linear temperature dependence of resistivity all the way down to $T = 0$.

The fluctuations of the order parameter, $\phi(q, \omega)$, are governed by an action,

$$S_{fl} = \int d^2q \int d\omega \phi^*(q, \omega) \Pi_{\text{inter}}^{-1}(q, \omega) \phi(-q, -\omega), \quad (6)$$

where Π_{inter} is the (interacting) interband polarizability of the system. When driven to the critical point, $\Pi_{\text{inter}}^{-1}(Q, 0) = 0$, i.e., the gap vanishes [this can be seen within a simple random phase approximation (RPA)-like theory], generically we would have

$$\Pi_{\text{inter}}^{-1} \sim \left[\omega^2 - c^2 \bar{q}^2 - i\gamma \frac{|\omega|}{|\bar{q}|} \right], \quad (7)$$

where $\bar{q} = q - Q$, and c and γ are constants denoting the speed of the fluctuation waves and the scale of damping. The singular $|\frac{\omega}{\bar{q}}|$ damping is a consequence of the presence of low-energy fermions and derives from the imaginary part of the noninteracting interband polarizability.

The noninteracting interband polarizability of the system is given by

$$\Pi_{\text{inter}}^0(q, \omega) = \sum_k \frac{f[\epsilon_c(k)] - f[\epsilon_v(k+q)]}{\omega + i\eta + \epsilon_c(k) - \epsilon_v(k+q)}$$

$$\times |\langle \psi_c(k) | \psi_v(k+q) \rangle|^2 + c \leftrightarrow v, \quad (8)$$

where f is the Fermi function and $|\psi_{c(v)}(k)\rangle$ is the Bloch wave function of the corresponding band in the mBZ. To see the Landau damping, in Fig. 6(a) we plot the imaginary part of Π_{inter}^0 as a function of ω for several values of q along the [1,0] direction. Note that $Q_1 \sim [0.016, 0]A^{-1}$ is along the [1,0] direction, so we will be crossing the exciton wave vector in the process. At low ω, the plots are linear and we extract a slope from this linear part of the graph. The slope is plotted as a function of q in Fig. 6(b). The slope diverges at $q = Q_1$, showing the singular nature of the Landau damping. We have checked, by taking momentum cuts along other directions passing through Q_1, that the divergence of the slope happens whenever we approach Q_1 along any direction, i.e., there is no difference in the scaling between directions along and perpendicular to the exciton/CDW wave vector (see Appendix A for details).

We can understand this further by constructing a simple model for the valence and conduction bands. The electron pocket of the conduction band is modeled by a Dirac dispersion centered around $k = 0$, i.e., $\epsilon_c(k) = v_F|k|$, while the hole pocket in the valence band is modeled by an inverted Dirac dispersion centered around Q, i.e., $\epsilon_v(k) = \epsilon_0 - v_F|k - Q|$, in Fig. 6(c). Here, ϵ_0 is the energy difference between the Dirac points. At the CNP, the chemical potential sits at $\mu = \epsilon_0/2$, giving a Fermi wave vector $k_F = \mu/v_F$ for electrons and holes. Usually, the orthogonality of the band wave functions as $q \rightarrow 0$ plays an important role in determining the low ω, q behavior of Π_{inter}^0 in graphene. However, here we are interested in Π_{inter}^0 near $q = Q$ where orthogonality considerations do not play a role. The band overlaps do not change the scaling of the various terms (although they can change the value of the coefficients such as γ, etc.). Hence we ignore band overlaps in
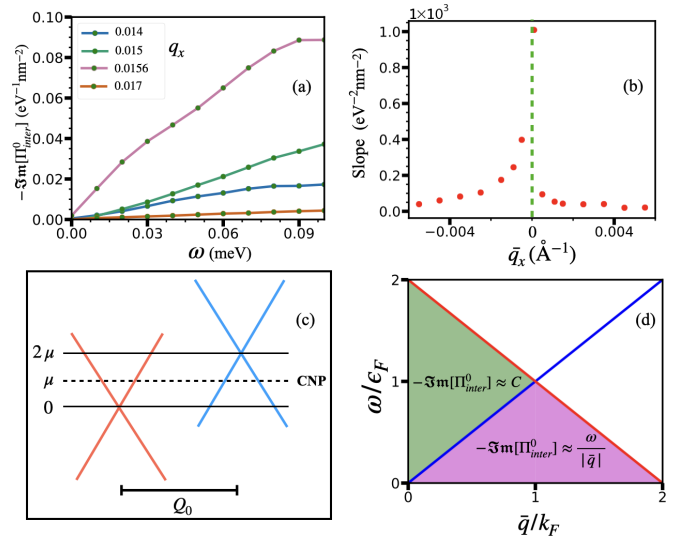

FIG. 6. (a) Imaginary part of the interband polarizability function plotted with frequency for different q_x values. Note that the direction of the $\bar{q}$ variation has been taken along the [1,0] direction, and around $Q_1 \approx (0.016, 0)$, which is the connecting wave vector between one of the e-h pockets. The low-frequency behavior is linear with the slope, showing a huge increase near Q_1. (b) The slope at different q_x from (a) is plotted here to show the divergence at $\bar{q} = Q_1$ (or $\bar{q} = 0$). (c) A simple theoretical model of the electron and hole pockets for calculating the interband polarizability of the system. The conduction (blue) and valence (red) Dirac bands are separated by Q_0 momentum inverted with respect to each other. The Dirac points are separated in energy by ϵ_0. At the CNP, the chemical potential $\mu = \epsilon_0/2$. (d) Schematic showing the regions in the $\bar{q} - \omega$ plane, where the imaginary part of the polarizability of the simple model shows (i) singular Landau damping $\text{Im}(\Pi_{\text{inter}}^0) \approx \frac{\omega}{|\bar{q}|}$ and (ii) a constant damping rate. The non-Fermi liquid behavior resulting from the Landau damping leads to the $T^{2/3}$ dependence of the resistivity.

our calculation of Π_{inter}^0. In this case, the polarization function can be calculated exactly and the detailed formulas are given in Appendix A. Near Q, the imaginary part of Π_{inter}^0 has the following form:

$$-\text{Im}\Pi_{\text{inter}}^0(q, \omega) \sim \frac{k_F^3}{4\pi\mu^2} \left| \frac{\omega}{\bar{q}} \right|; (\omega < v_F\bar{q} \text{ when } \bar{q} < k_F) \text{ or}$$

$$(\omega < \epsilon_0 - v_F\bar{q} \text{ when } \bar{q} > k_F),$$

$$\sim \frac{k_F^2}{8\mu} \quad ; \epsilon_0 - v_F\bar{q} > \omega > v_F\bar{q}. \quad (9)$$

Thus both the numerical calculation on the full model and the analytic calculation with the simple model show the presence of the singular Landau damping around $q \sim Q$. The Landau damped fluctuations have an energy momentum relation $\omega \sim \bar{q}^3$, leading to a density of states $\rho(\omega) \sim \omega^{-1/3}$. The scattering of electrons by these fluctuations leads to a single-particle scattering rate,

$$\Gamma_{qP} \propto \int_0^\omega d\omega' \rho(\omega') \sim \omega^{2/3} \text{ at } T = 0, \quad (10)$$

$$\propto \int_0^{\omega_c} d\omega \rho(\omega) \coth\left(\frac{\omega}{2T}\right) \sim T^{2/3} \text{ at } T \neq 0, \quad (11)$$

where ω_c is a cutoff below which the long wavelength description mentioned above holds with the condition $\omega_c \gg T$. The damping rate $\omega^{2/3}$ is larger than the energy of excitations leading to non-Fermi liquid behavior. Since the Fermi pockets in tDBLG near the CNP are small, scattering at all angles contributes to transport and hence the transport scattering rate $\Gamma_{tr} \sim \Gamma_{qp} \sim T^{2/3}$. This is the origin of the $T^{2/3}$ dependence of resistance in the system. Thus the sublinear temperature dependence is a reflection of an underlying non-Fermi liquid state in a quantum critical metal. We note that such a Fermi golden rule calculation assumes that once the momentum is lost to the Landau damped fluctuations, it is never recovered by the electrons. If one considers the coherent process where the fluctuations simply mediate scattering between electrons, several authors [75–79] have shown that in a single Fermi surface case, the coefficient of the $T^{2/3}$ term in transport vanishes in two dimensions for convex Fermi surfaces. In our case, that would correspond to an exact particle-hole symmetry, i.e., the particle and hole Fermi surfaces are exactly aligned and the effective mass and scattering rate of the particles and holes are the same. However, in tDBLG, particle-hole symmetry is broken and the Fermi surfaces are not exactly aligned. More importantly, the mass and the scattering rate of the particles and holes are very different. This can be seen from the fact that in experiments, the resistance as a function of carrier density is particle-hole asymmetric (roughly by a factor of $\sim$1.5–2.0) [33]. The effective mass calculated from band dispersions also shows a similar magnitude of asymmetry. Thus our case is closer to the *s-d* model discussed in Ref. [75], where a $T^{2/3}$ resistivity would be recovered.

Starting with the work of Hertz and Millis [35,36], the non-Fermi liquid behavior of itinerant quantum critical systems has been studied in the context of high-temperature superconductivity [39,40,80] for the antiferromagnetic metal [38,81,82] and for the nematic transition in metals [34,83], using sophisticated renormalization group techniques. The general conclusion is that the imaginary part of the electron self-energy is $\sim \omega^{2/3}$ when the order parameter is at zero wave vector [34] (as in nematic transition), while we get a $\sim \omega^{1/2}$ dependence for a finite Q wave-vector order like spin density waves [42]. We note that in our case, the finite wave vector relates the center of the electron pocket to the center of the hole pocket, so the electron and hole Fermi surfaces lie on top of each other when shifted by this wave vector. Thus, although the CDW is formed at finite wave vector, our itinerant quantum criticality is similar to the nematic case with effective $q = 0$ and we recover the $\sim \omega^{2/3}$ scaling of the self-energy.

In the experiments, it is seen that the resistivity shows a linear temperature dependence above $T = 10$ K. We note that the Fermi temperature corresponding to the e-h pockets is $T_F \sim 20$–25 K and one would expect quantum behaviors to vanish beyond this temperature. For a two-dimensional system with small Fermi surfaces, a more relevant scale would be the effective "Bloch Gruneissen" temperature of these critical fluctuations, i.e., their energy for $\bar{q} \sim 2k_F$. While this requires interaction renormalized estimates of γ and c, which are beyond the scope of this paper, one would expect this temperature to be lower than T_F. If we assume that beyond $T = 10$ K these fluctuations are classical, we can obtain the linear temperature dependence of resistivity in this regime.

As we move away from the CNP on either side, the mismatch between the electron and hole Fermi surfaces increases, and the Landau damping would be shifted to finite $\bar{q} > \Delta k_F$, where Δk_F is the mismatch of the Fermi wave vectors of the electron and hole pockets. In this case, the low-temperature behavior of resistivity would deviate from the $T^{2/3}$ scaling. Assuming the $|\omega/\bar{q}|$ scaling of the Landau damping is cut off on the scale of Δk_F, i.e., it scales as $|\omega/\Delta k_F|$, one would get a linear T dependence of the resistivity. However, this exponent would be strongly influenced by disorder and Fermi surface anisotropies. In general, one would expect the exponent to increase as one goes away from the CNP. Once the simultaneous presence of electron and hole pockets vanishes at larger doping, one gets back the standard T^2 scaling of the Fermi liquid theory.

VI. CONCLUSION

Strong electronic interactions determine the plethora of symmetry-broken phases in magic angle tBLG and tTLG. In contrast, tDBLG is usually thought of as a conventional metal in the absence of electric/magnetic fields. The metallicity of magic angle tDBLG near the CNP comes from the overlap of flat conduction and valence bands, which creates small electron and hole pockets at the Fermi surface.

In this paper, we have considered the possible effects of Coulomb interaction on these small e-h pockets in the compensated semimetal near the CNP. We show that the interactions lead to the formation of indirect excitons (i.e., particle-hole pairs with finite momenta). The condensation of such pairs leads to the formation of CDW states. We show that for a reasonable range of interaction parameters, this ordered state has reorganized Fermi pockets and hence metallic behavior is expected. However, the density of electronic states is strongly renormalized in the process. The inverse density of states at the Fermi level shows peaks at finite doping on either side of the CNP. This can explain the peaks in the resistance as a function of density seen in recent low-temperature experiments [33]. We further show that the Landau damped critical fluctuations of the excitonic order can give rise to non-Fermi liquid behavior of the electrons with a scattering rate $\Gamma \sim T^{2/3}$. For systems such as tDBLG, with small Fermi pockets, this can give rise to sublinear $T^{2/3}$ resistance seen in recent experiments [33]. Although we have used a simple mean-field (MF) approximation to treat the system, the fact that the MF theory can explain the two distinct and unusual features of the low-T transport data in tDBLG gives us confidence that it is qualitatively correct in describing the system.

We would like to note that we have neglected the intraband e-e interaction while considering the formation of excitons in our calculation. This is justified by the fact that if one works in an electron coordinate for the conduction band and in a hole coordinate for the valence band, one will immediately realize that the interband e-e interaction leads to an attractive interaction, whereas the intraband e-e gives a repulsive interaction. The attractive interaction is usually large compared to its counterpart and leads to instability in the system. The repulsive intraband interaction might change the quantitative nature of the itinerant Fermi liquid, but cannot change the nature of the singularity brought by the exciton condensate. This

argument is also backed by the fact that unlike tBLG [66–68], this tDBLG system has much less doping-dependent band structure deformation [69] from Hartree interaction. Thus it is sufficient to use a noninteracting band structure and add an interband attractive type of quasielectron quasihole interaction to study the nontrivial phases of the system.

Our theoretical predictions thus strongly indicate that the effect of excitonic/CDW order and its fluctuations has already been observed through the non-Fermi liquid temperature dependence of the resistivity. A hallmark of CDW insulators is the current produced by the sliding mode when the order is depinned by finite energy probes (nonlinear/AC conductivity). However, in a metallic system such as tDBLG, these contributions would be masked by the usual single-particle contributions. We believe that the fluctuations of the finite particle-hole condensate should give additional contributions to current noise, but we leave this calculation for a future manuscript. There are other systems in the moiré family such as mono-bilayer graphene [84] and mono-trilayer graphene [85] which host similar e-h pockets at the Fermi surface and metallic states at the CNP like tDBLG. In general, one would expect similar electron-hole pairing in these systems; however, their bandwidth is larger than magic angle tDBLG and they would have a weaker interaction to the kinetic energy ratio. Thus the energy scales for exciton formation may be exponentially smaller in these cases. We note that till now there are no experimental data to either support or disprove exciton formation in these systems.

ACKNOWLEDGMENTS

APPENDIX A: INTERBAND POLARIZABILITY AND LANDAU DAMPING

We are interested in the low-energy dispersion of valence and conduction bands in tDBLG, especially the modes which constitute the electron and hole pockets near the CNP. For these modes, the energy dispersion can be approximated as two Dirac cones separated in momentum and energy, as shown in Fig. 6(c). We use the hole band of the Dirac cone inverted around the higher Dirac point and the electron band around the lower Dirac point as

$$
\begin{aligned}
\epsilon_{\mathbf{k}}^c &= v_F |\mathbf{k}|, \\
\epsilon_{\mathbf{k}}^v &= 2\mu - v_F |\mathbf{k} - \mathbf{Q}_0|.
\end{aligned}
\tag{A1}
$$

Here, $\epsilon_k^{c(v)}$ is the energy dispersion of the conduction (valence) band, μ is the chemical potential at the CNP, v_F denotes the Fermi velocity of the effective Dirac points, and the momentum separation wave vector between two Dirac cones is given by $\mathbf{Q}_0$. Also, one can note that the exciton order parameter $\Delta(\mathbf{q}) \sim \sum_{\mathbf{k}} \langle C_{\mathbf{k}}^{\dagger c} C_{\mathbf{k+q}}^v \rangle$, so its fluctuations, $\chi_{\Delta\Delta}(q, t - t') = i\theta(t - t') \sum_{\mathbf{kk'}} \langle [C_{\mathbf{k}}^{c\dagger}(t) C_{\mathbf{k+q}}^v(t), C_{\mathbf{k'}}^{v\dagger}(t') C_{\mathbf{k'-q}}^c(t')] \rangle$, are related to the noninteracting interband polarizability,

$$
\Pi_{cv}^0(\mathbf{q}, \omega) = \sum_{\mathbf{k} \in mBZ} \frac{f(\epsilon_{\mathbf{k}}^c - \mu) - f(\epsilon_{\mathbf{k+q}}^v - \mu)}{\omega + \epsilon_{\mathbf{k}}^c - \epsilon_{\mathbf{k+q}}^v} |\langle \psi_{\mathbf{k}}^c | \psi_{\mathbf{k+q}}^v \rangle|^2,
\tag{A2}
$$

where the total polarizability $\Pi_{inter}^0 = \Pi_{cv}^0 + \Pi_{vc}^0$. Usually the orthogonality of the band wave functions as $q \to 0$ plays an important role in determining the low ω, q behavior of Π_{inter}^0 in graphene. However, here we are interested in Π_{inter}^0 near $q = Q$, where orthogonality considerations do not play a role. The band overlaps do not change the scaling of various terms. Hence we can drop the term $|\langle \psi_{\mathbf{k}}^c | \psi_{\mathbf{k+q}}^v \rangle|^2$ from Eq. (A2) and write it as

$$
\begin{aligned}
\Pi_{cv}^0(\mathbf{q}, \omega) \sim &\int \frac{d^2\mathbf{k}}{4\pi^2} \frac{f(\epsilon_{\mathbf{k}}^c - \mu)}{\omega + \epsilon_{\mathbf{k-\bar{q}}}^c + \epsilon_{\mathbf{k}}^c - 2\mu} \\
&- \int \frac{d^2\mathbf{k}}{4\pi^2} \frac{1 - f(\epsilon_{\mathbf{k}}^c - \mu)}{\omega + \epsilon_{\mathbf{k}}^c + \epsilon_{\mathbf{k+\bar{q}}}^c - 2\mu},
\end{aligned}
\tag{A3}
$$

where $\bar{\mathbf{q}} = \mathbf{q} - \mathbf{Q}_0$. Now using dimensionless parameters, $X = k/k_F$, $Y = \bar{q}/k_F$, and $Z = \omega/\mu$, Eq. (A3) can be rewritten as

$$
\begin{aligned}
\Pi_{cv}^0(\mathbf{q}, \omega) \sim -\frac{k_F^2}{4\pi^2 \mu} \bigg[&-\int_0^1 X dX \int d\phi \frac{1}{Z - 2 + X + \sqrt{X^2 + Y^2 - 2XY\cos\phi}} \\
&+ \int_1^\Lambda X dX \int d\phi \frac{1}{Z - 2 + X + \sqrt{X^2 + Y^2 + 2XY\cos\phi}} \bigg].
\end{aligned}
$$

Here, ϕ is the azimuthal angle between $\mathbf{k}$ and $\bar{\mathbf{q}}$, and Λ is an ultraviolet cutoff. We note that the Landau damping we calculate is a low-energy property, which is independent of Λ. We are interested in the imaginary part of the polarizability, $\Pi'' \equiv \mathrm{Im}[\Pi_{cv}^0]$, which then becomes

$$
\begin{aligned}
\Pi'' \sim -\frac{k_F^2}{4\pi\mu} \bigg\{ &\int_0^1 X dX \int_{-1}^{+1} \frac{du}{\sqrt{1 - u^2}} \delta[Z - 2 + X + \sqrt{X^2 + Y^2 - 2XYu}] \\
&- \int_1^\Lambda X dX \int_{-1}^{+1} \frac{du}{\sqrt{1 - u^2}} \delta[Z - 2 + X + \sqrt{X^2 + Y^2 + 2XYu}] \bigg\}.
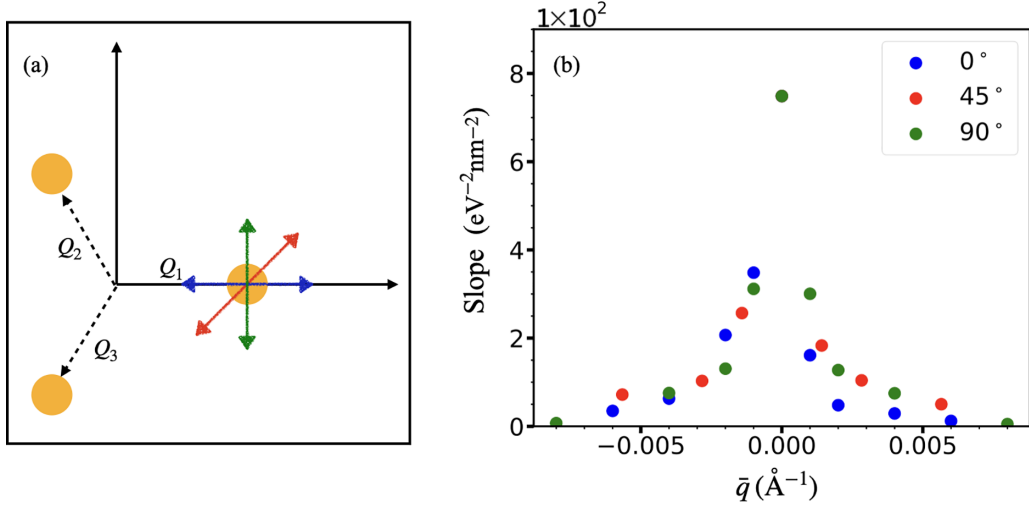\end{aligned}
$$

FIG. 7. (a) A schematic of the three C_3 symmetric critical points in the momentum space. Around the Q_1 point, we have taken the q-cuts of $\frac{d\,\Pi''}{d\omega}|_{\omega\to 0}$ along the directions drawn and plotted them in (b). Notice that q has been scaled to $\bar{q} = q - Q_1$. The slope along all three directions, [1,0] (blue), [1,1] (red), and [0,1] (green), shows divergence at the critical point and a very small anisotropy on top of the isotropic background. One thing to note is that for (b), we have used a different set of parameters (momentum grid 350×350 and broadening $\eta = 0.05$ meV) than for Fig. 6(b), where we used momentum grid 800×800 and broadening $\eta = 0.02$ meV. That is the reason the divergence scale of the slopes is different for these two figures, which is expected.

Here, $u = \cos\phi$. This azimuthal integral can be done analytically to get

$$\Pi'' \sim -\frac{k_F^2}{4\pi\mu}\left[\int_0^1 - \int_1^\Lambda\right]X\,dX\,\frac{\theta\{4X^2Y^2 - [X^2 + Y^2 - (2 - Z - X)^2]^2\}}{\sqrt{4X^2Y^2 - [X^2 + Y^2 - (2 - Z - X)^2]^2}},$$

which can also be written as

$$\Pi'' \sim -\frac{k_F^2}{4\pi\mu}\left[\int_0^1 - \int_1^\Lambda\right]X\,dX\,\frac{\theta[\{(2 - Z)^2 - Y^2\}(X^+ - X)(X - X^-)]}{\sqrt{4\{(2 - Z)^2 - Y^2\}(X^+ - X)(X - X^-)}}, \tag{A4}$$

where $X^\pm = [(2 - Z) \pm Y]/2$. We will work with $Y, Z > 0$ and $Y, Z \ll 1$ so that $Z < 2$ and $Y < 2 - Z$. In this case, $X^+ > X^- > 0$. Now, depending on the value of Y, Z, we can have different regions in the phase space where the integrals take qualitatively different forms, as follows.

Case (i). $0 < Z < 1$ and $0 < Y < Z$
or $1 < Z < 2$ and $0 < Y < 2 - Z$,

$$-\Pi'' \sim \frac{k_F^2 (2 - Z)}{16\mu\sqrt{(2 - Z)^2 - Y^2}}$$

$$\approx \frac{k_F^2}{16\mu}; \ (Y \ll 2 - Z). \tag{A5}$$

Case (ii). $0 < Z < 1$ and $Z < Y < 2 - Z$,

$$-\Pi'' \sim \frac{k_F^2}{8\pi\mu\sqrt{(2 - Z)^2 - Y^2}}$$

$$\times \left[(2 - Z)\ \sin^{-1}\left(\frac{Z}{Y}\right) - \sqrt{Y^2 - Z^2}\right]$$

$$\approx \frac{k_F^2}{8\pi\mu}\frac{Z}{Y}; \ (Y \to 0, Z/Y \to 0)$$

$$\sim \frac{k_F^3}{8\pi\mu^2}\frac{|\omega|}{|\bar{q}|}. \tag{A6}$$

Therefore, we analytically show the Landau damping factor $\left(\frac{|\omega|}{|\bar{q}|}\right)$ arising from the imaginary part of the interband polarizability function assuming two simple Dirac bands separated from each other in energy and momentum space. One can easily see that Π_{vc}^0 will give the same contribution. Collecting all these,

$$-\operatorname{Im}\Pi_{\text{inter}}^0(q, \omega) \sim \frac{k_F^2}{8\mu}; \ Y < Z < 2 - Y \text{ for } Y < 1 \tag{A7}$$

$$\sim \frac{k_F^3}{4\pi\mu^2}\frac{|\omega|}{|\bar{q}|}; \ (Z < Y \text{ for } Y < 1) \text{ or } (Z < 2 - Y \text{ for } Y > 1). \tag{A8}$$

As shown in the main text, the numerical evaluation of Π'' using the actual tDBLG dispersion and wave functions also give rise to similar singular damping. In the main text, we looked at $\frac{d\,\Pi''(q,\omega)}{d\omega}|_{\omega\to 0}$ as a function of q. Here, in Fig. 7(b), we additionally plot the slope $\frac{d\,\Pi''}{d\omega}|_{\omega\to 0}$ along a cut in q which passes through Q_0 and moves along the [0,1] (90°) and [1,1] (45°) directions [the directions are schematically shown in Fig. 7(a)]. We see that the slope diverges at Q_0 irrespective of the direction in which it is approached. Thus the Landau damping has only small anisotropies riding on an isotropic
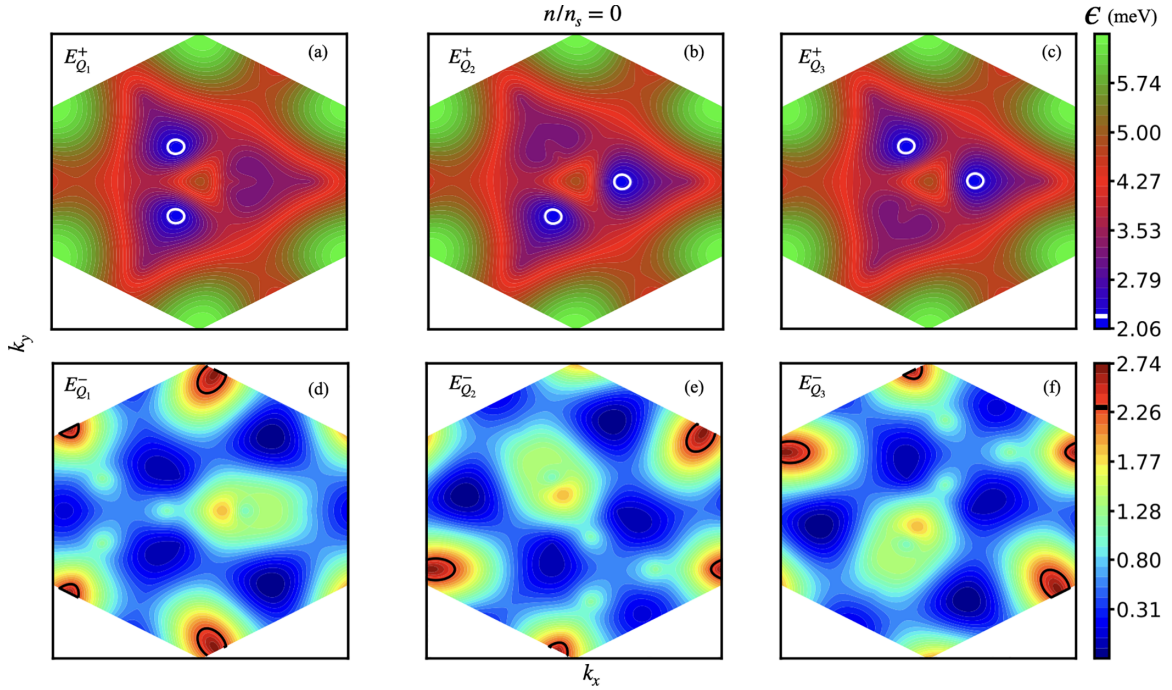
FIG. 8. (a)–(c) Color plots of the renormalized conduction bands due to the presence of excitonic order parameters for the three e-h pocket connecting wave vectors $Q_{1(2)(3)}$, respectively, at the CNP. (d)–(f) The renormalized valence bands at the CNP. The solid lines represent the Fermi surface at the CNP. Here both the electron and hole pockets contribute to the resistivity of the system.

background, even though the Fermi velocities at the Dirac points are anisotropic. This isotropy is important for scaling arguments used to explain $T^{2/3}$ resistivity.

APPENDIX B: BAND RENORMALIZATION DUE TO EXCITON FORMATION

In the main text, we had shown that the presence of excitonic order leads to the formation of six minibands out of the original tDBLG dispersion. Here, we present the detailed dispersion of these six bands and how they change with density around the CNP in Figs. 8–10. In Fig. 8, we plot the dispersion of the six bands (three conduction bands in the top row and three valence bands in the bottom row) at the CNP as a color plot. The electron and hole Fermi surfaces are shown as solid lines. Note that the dispersion of the bands is not C_3 symmetric for individual Q_i's. The e-h pocket that is coupled by the excitonic order is gapped out. Figure 9 plots the same dispersion at $n/n_s = 0.06$. One can see that the electron pockets have grown, while the hole pockets have shrunk to zero. Finally, Fig. 10 plots the dispersion at $n/n_s = 0.10$. The hole pockets from the valence band have vanished and electron pockets are still present. But additional electron pockets appear in the conduction band. The extra density of states from these new pockets lead to a suppression of resistivity, giving rise to the two-peak structure in the resistivity vs density data [33].

APPENDIX C: LANDAU-GINZBURG (LG) ANALYSIS FOR MEAN FIELD

In this Appendix, we write a Landau-Ginzburg theory for three charge density order parameters $\Delta_{1,2,3}$, where Δ_i is the mean-field parameter for the ith e-h pocket in the 3-Q model

that we have considered. which carry wave vectors $\mathbf{Q}_i$. The free energy density in this case must be invariant under the U(1) symmetry that gives phase rotation to the conduction and valence electron operators separately; it also needs to be translationally invariant. In addition, the C_3 symmetry within a valley needs to be respected. Note that since $\mathbf{Q}_1 + \mathbf{Q}_2 + \mathbf{Q}_3 = 0$, the terms that conserve translation invariance up to fourth order in the order parameters is given by

$$F = -|r| \sum_i |\Delta_i|^2 + \lambda_2 \sum_i |\Delta_i|^4 + \lambda_3 \sum_{i \neq j} |\Delta_i|^2 |\Delta_j|^2.$$
(C1)

Note that C_3 symmetry implies that the mass terms and the self-couplings for the three order parameters must be the same. Minimization of the free energy with respect to Δ_i^* leads to

$$\frac{\delta F}{\delta \Delta_i^*} = -|r| \Delta_i + 2\lambda_2 \Delta_i |\Delta_i|^2 + \lambda_3 \sum_{j \neq i} \Delta_i |\Delta_j|^2 = 0. \quad \text{(C2)}$$

The above equation gives the following conditions for non-trivial values of Δ_i (the trivial solution $\Delta_i = 0$ is always a possibility):

$$2\lambda_2 |\Delta_1|^2 + \lambda_3 (|\Delta_2|^2 + |\Delta_3|^2) = |r|, \quad \text{(C3)}$$

$$2\lambda_2 |\Delta_2|^2 + \lambda_3 (|\Delta_3|^2 + |\Delta_1|^2) = |r|, \quad \text{(C4)}$$

$$2\lambda_2 |\Delta_3|^2 + \lambda_3 (|\Delta_1|^2 + |\Delta_2|^2) = |r|. \quad \text{(C5)}$$

We now look at different patterns of solutions for these equations and consider the free energy of those states. We note that these equations are independent of the relative phases of the order parameters and cannot determine them. The
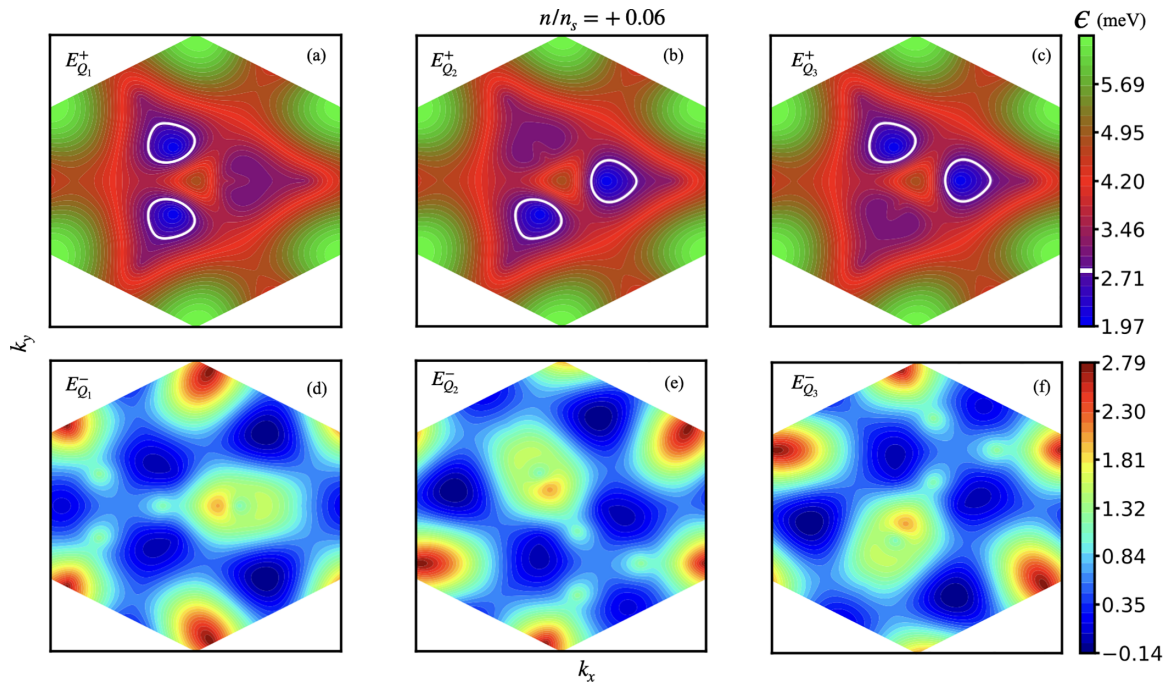
FIG. 9. Similar to Fig. 8, here we have plotted the exciton bands for density $n/n_s = 0.06$. One can notice that the hole pockets have vanished, which explains the suppression of the density of states which leads to an increase in the resistivity.

first term that cares about relative phases has six powers of order parameters (and is doped here since three order parameters multiplied together can give a translationally invariant quantity).

Case (i). $\Delta_1, \Delta_2, \Delta_3 \neq 0$.
Subcase (i). $\Delta_1 = \Delta_2 = \Delta_3 = \Delta$.

Using this in Eq. (C3), we get $|\Delta|^2 = \frac{|r|}{2(\lambda_2 + \lambda_3)}$. Hence the free energy for this case becomes

$$F_{\Delta\Delta\Delta} = \frac{-3|r|^2}{4(\lambda_2 + \lambda_3)}. \tag{C6}$$

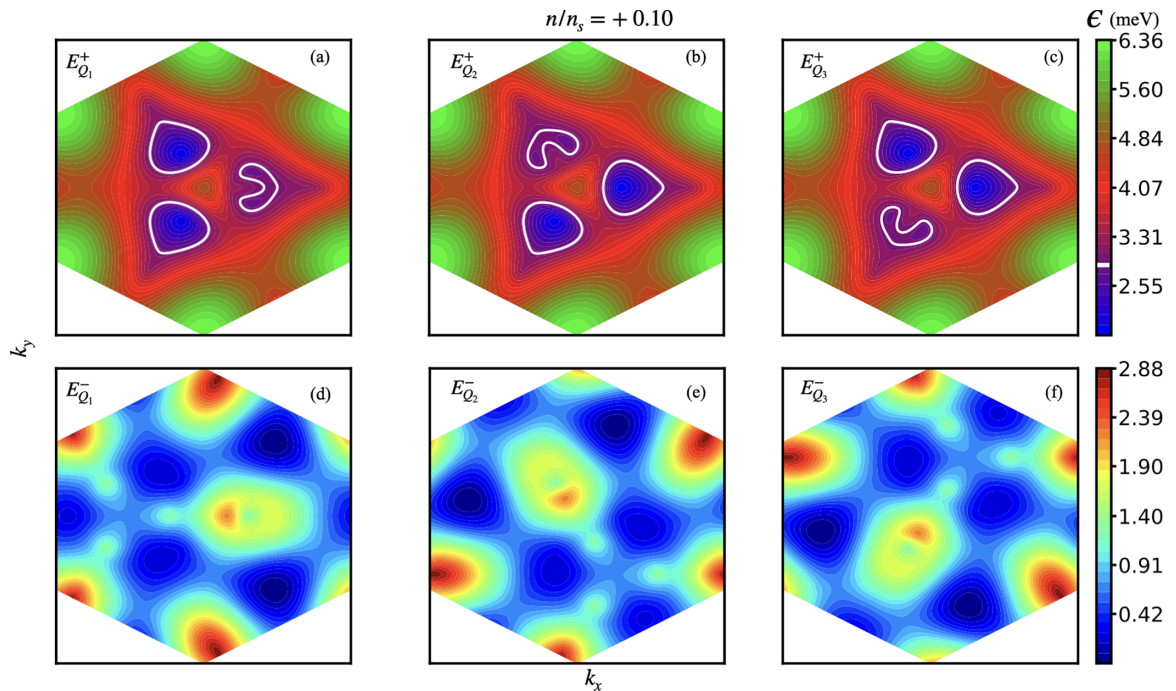*Subcase (ii).* $\Delta_1 = \Delta_2 = \Delta \neq \Delta_3$. Let $|\Delta_3|^2 = |\Delta|^2 + \epsilon$.

FIG. 10. Similar to Fig. 8, here we have plotted the exciton bands for density $n/n_s = 0.10$. Here one can notice that extra electron pockets have emerged from higher bands, which causes the increment of the density of states that leads to a decrease in the resistivity. Figures 8–10 thus explain the double-peak feature seen in recent experiments [33].

Using this in Eq. (C3), we get

$$2|\Delta|^2(\lambda_2 + \lambda_3) + \lambda_3\epsilon = |r|. \quad (C7)$$

Similarly, from Eq. (C5), we get

$$2|\Delta|^2(\lambda_2 + \lambda_3) + 2\lambda_2\epsilon = |r|. \quad (C8)$$

Subtracting Eq. (C8) from Eq. (C7), we get $(\lambda_3 - 2\lambda_2)\epsilon = 0$. Therefore, to get a nontrivial solution of ϵ, we need a very fine-tuned condition of λ_i's. Hence this case can be neglected in general.

Subcase (iii). $\Delta_1 \neq \Delta_2 \neq \Delta_3$. Let $|\Delta_1|^2 = |\Delta|^2$, $|\Delta_2|^2 = |\Delta|^2 + \epsilon_1$, and $|\Delta_3|^2 = |\Delta|^2 + \epsilon_2$.

Subtracting Eq. (C3) from Eq. (C4), we get $(2\lambda_2 - \lambda_3)(|\Delta_2|^2 - |\Delta_1|^2) = 0$. Then, using the above definition of Δ_i's, we get $(2\lambda_2 - \lambda_3)\epsilon_1 = 0$. Similarly, subtracting Eq. (C3) from Eq. (C5), we get $(2\lambda_2 - \lambda_3)(|\Delta_3|^2 - |\Delta_1|^2) = 0$. Then, using the above definition of Δ_i's, we get $(2\lambda_2 - \lambda_3)\epsilon_2 = 0$. Therefore, we need the same stringent condition of λ_i's to get a nontrivial solution of ϵ_1 and ϵ_2. Hence this case can also be neglected in general.

Case (ii). $\Delta_1, \Delta_2 \neq 0$ and $\Delta_3 = 0$.

Subcase (i). $\Delta_1 = \Delta_2 = \Delta$.

Using this in Eq. (C3), we get $|\Delta|^2 = \frac{|r|}{2\lambda_2 + \lambda_3}$. Hence the free energy for this case becomes

$$F_{\Delta\Delta 0} = \frac{-|r|^2}{2\lambda_2 + \lambda_3}. \quad (C9)$$

In order to show that all three e-h pockets having same magnitude of mean field is the minimum energy solution we need, $\frac{|F_{\Delta\Delta 0}|}{|F_{\Delta\Delta\Delta}|} < 1$. This leads to the condition

$$\frac{4(\lambda_2 + \lambda_3)}{3(2\lambda_2 + \lambda_3)} < 1 \Rightarrow \frac{\lambda_3}{\lambda_2} < 2. \quad (C10)$$

Subcase (ii). $\Delta_1 \neq \Delta_2$ and $\Delta_3 = 0$. Let $|\Delta_1|^2 = |\Delta|^2$, $|\Delta_2|^2 = |\Delta|^2 + \epsilon$.

Using this in Eq. (C3), we get

$$2\lambda_2|\Delta|^2 + \lambda_3(|\Delta|^2 + \epsilon) = |r|. \quad (C11)$$

And from Eq. (C4), we get

$$2\lambda_2(|\Delta|^2 + \epsilon) + \lambda_3|\Delta|^2 = |r|. \quad (C12)$$

Subtracting Eq. (C12) from Eq. (C11), we get $(\lambda_3 - 2\lambda_2)\epsilon = 0$. Therefore, following our previous argument, this case can also be neglected in general.

Case (iii). $\Delta_1 = \Delta \neq 0$ and $\Delta_2 = \Delta_3 = 0$.

Using this in Eq. (C3), we get $|\Delta|^2 = \frac{|r|}{2\lambda_2}$. Hence the free energy for this case becomes

$$F_{\Delta 00} = \frac{-|r|^2}{4\lambda_2}. \quad (C13)$$

Again, in order to show that all three e-h pockets having same magnitude of mean field is the minimum energy solution we need, $\frac{|F_{\Delta 00}|}{|F_{\Delta\Delta\Delta}|} < 1$. This leads to the condition

$$\frac{\lambda_2 + \lambda_3}{3\lambda_2} < 1 \Rightarrow \frac{\lambda_3}{\lambda_2} < 2. \quad (C14)$$

Therefore, if $\frac{\lambda_3}{\lambda_2} < 2$, the minimum free energy solution of the LG problem is the case where all Δ_i's are equal in magnitude, which was our ansatz in the main text. This is true as long as the quartic coupling between order parameters with different wave vectors (λ_3) is less than twice the quartic coupling between the order parameter with same wave vector (λ_2). We note that these couplings are, at best, equal to each other; more likely, the coupling between the order parameters with different Q is smaller since they require connecting electron pockets with hole pockets further from them. Thus the equal amplitude solution is the lowest-energy solution.

[1] R. Bistritzer and A. H. MacDonald, Moiré bands in twisted double-layer graphene, Proc. Natl. Acad. Sci. **108**, 12233 (2011).

[2] J. M. B. Lopes dos Santos, N. M. R. Peres, and A. H. Castro Neto, Continuum model of the twisted graphene bilayer, Phys. Rev. B **86**, 155449 (2012).

[3] M. Koshino, N. F. Q. Yuan, T. Koretsune, M. Ochi, K. Kuroki, and L. Fu, Maximally Localized Wannier Orbitals and the Extended Hubbard Model for Twisted Bilayer Graphene, Phys. Rev. X **8**, 031087 (2018).

[4] J. M. B. Lopes dos Santos, N. M. R. Peres, and A. H. Castro Neto, Graphene Bilayer with a Twist: Electronic Structure, Phys. Rev. Lett. **99**, 256802 (2007).

[5] B. A. Bernevig, Z.-D. Song, N. Regnault, and B. Lian, Twisted bilayer graphene. I. Matrix elements, approximations, perturbation theory, and a $k \cdot p$ two-band model, Phys. Rev. B **103**, 205411 (2021).

[6] S. Carr, D. Massatt, S. Fang, P. Cazeaux, M. Luskin, and E. Kaxiras, Twistronics: Manipulating the electronic properties of two-dimensional layered structures through their twist angle, Phys. Rev. B **95**, 075420 (2017).

[7] G. Tarnopolsky, A. J. Kruchkov, and A. Vishwanath, Origin of Magic Angles in Twisted Bilayer Graphene, Phys. Rev. Lett. **122**, 106405 (2019).

[8] L. Zou, H. C. Po, A. Vishwanath, and T. Senthil, Band structure of twisted bilayer graphene: Emergent symmetries, commensurate approximants, and Wannier obstructions, Phys. Rev. B **98**, 085435 (2018).

[9] N. R. Chebrolu, B. L. Chittari, and J. Jung, Flat bands in twisted double bilayer graphene, Phys. Rev. B **99**, 235417 (2019).

[10] P. Mohan, U. Ghorai, and R. Sensarma, Trigonal warping, satellite Dirac points, and multiple field tuned topological transitions in twisted double bilayer graphene, Phys. Rev. B **103**, 155149 (2021).

[11] Y. Cao, V. Fatemi, A. Demir, S. Fang, S. L. Tomarken, J. Y. Luo, J. D. Sanchez-Yamagishi, K. Watanabe, T. Taniguchi, E. Kaxiras, R. C. Ashoori, and P. Jarillo-Herrero, Correlated insulator behaviour at half-filling in magic-angle graphene superlattices, Nature (London) **556**, 80 (2018).

[12] Y. Cao, V. Fatemi, S. Fang, K. Watanabe, T. Taniguchi, E. Kaxiras, and Jarillo-Herrero, Unconventional superconductivity

in magic-angle graphene superlattices, Nature (London) **556**, 43 (2018).

[13] M. Yankowitz, S. Chen, H. Polshyn, Y. Zhang, K. Watanabe, T. Taniguchi, D. Graf, A. F. Young, and C. R. Dean, Tuning superconductivity in twisted bilayer graphene, Science **363**, 1059 (2019).

[14] J. M. Park, Y. Cao, K. Watanabe, T. Taniguchi, and P. Jarillo-Herrero, Tunable strongly coupled superconductivity in magic-angle twisted trilayer graphene, Nature (London) **590**, 249 (2021).

[15] Z. Hao, A. M. Zimmerman, P. Ledwith, E. Khalaf, D. H. Najafabadi, K. Watanabe, T. Taniguchi, A. Vishwanath, and P. Kim, Electric field-tunable superconductivity in alternating-twist magic-angle trilayer graphene, Science **371**, 1133 (2021).

[16] J. M. Park, Y. Cao, L. Xia, S. Sun, K. Watanabe, T. Taniguchi, and P. Jarillo-Herrero, Magic-angle multilayer graphene: A robust family of moiré superconductors, arXiv:2112.10760.

[17] Y. Cao, D. Rodan-Legrain, O. Rubies-Bigorda, J. M. Park, K. Watanabe, T. Taniguchi, and P. Jarillo-Herrero, Tunable correlated states and spin-polarized phases in twisted bilayer-bilayer graphene, Nature (London) **583**, 215 (2020).

[18] G. W. Burg, J. Zhu, T. Taniguchi, K. Watanabe, A. H. MacDonald, and E. Tutuc, Correlated Insulating States in Twisted Double Bilayer Graphene, Phys. Rev. Lett. **123**, 197702 (2019).

[19] P. C. Adak, S. Sinha, U. Ghorai, L. D. V. Sangani, K. Watanabe, T. Taniguchi, R. Sensarma, and M. M. Deshmukh, Tunable bandwidths and gaps in twisted double bilayer graphene on the verge of correlations, Phys. Rev. B **101**, 125428 (2020).

[20] A. Mishchenko, J. S. Tu, Y. Cao, R. V. Gorbachev, J. R. Wallbank, M. T. Greenaway, V. E. Morozov, S. V. Morozov, M. J. Zhu, S. L. Wong, F. Withers, C. R. Woods, Y.-J. Kim, K. Watanabe, T. Taniguchi, E. E. Vdovin, O. Makarovsky, T. M. Fromhold, V. I. Fal'ko, A. K. Geim *et al.*, Twist-controlled resonant tunnelling in graphene/boron nitride/graphene heterostructures, Nat. Nanotechnol. **9**, 808 (2014).

[21] Z. Zhang, Y. Wang, K. Watanabe, T. Taniguchi, K. Ueno, E. Tutuc, and B. J. LeRoy, Flat bands in twisted bilayer transition metal dichalcogenides, Nat. Phys. **16**, 1093 (2020).

[22] L. Wang, E.-M. Shih, A. Ghiotto, L. Xian, D. A. Rhodes, C. Tan, M. Claassen, D. M. Kennes, Y. Bai, B. Kim, K. Watanabe, T. Taniguchi, X. Zhu, J. Hone, A. Rubio, A. N. Pasupathy, and C. R. Dean, Correlated electronic phases in twisted bilayer transition metal dichalcogenides, Nat. Mater. **19**, 861 (2020).

[23] X. Lu, P. Stepanov, W. Yang, M. Xie, M. A. Aamir, I. Das, C. Urgell, K. Watanabe, T. Taniguchi, G. Zhang, A. Bachtold, A. H. MacDonald, and D. K. Efetov, Superconductors, orbital magnets and correlated states in magic-angle bilayer graphene, Nature (London) **574**, 653 (2019).

[24] X. Liu, Z. Hao, E. Khalaf, J. Y. Lee, Y. Ronen, H. Yoo, D. H. Najafabadi, K. Watanabe, T. Taniguchi, A. Vishwanath, and P. Kim, Tunable spin-polarized correlated states in twisted double bilayer graphene, Nature (London) **583**, 221 (2020).

[25] K. P. Nuckolls, M. Oh, D. Wong, B. Lian, K. Watanabe, T. Taniguchi, B. A. Bernevig, and A. Yazdani, Strongly correlated Chern insulators in magic-angle twisted bilayer graphene, Nature (London) **588**, 610 (2020).

[26] A. L. Sharpe, E. J. Fox, A. W. Barnard, J. Finney, K. Watanabe, T. Taniguchi, M. A. Kastner, and D. Goldhaber-

Gordon, Emergent ferromagnetism near three-quarters filling in twisted bilayer graphene, Science **365**, 605 (2019).

[27] M. Oh, K. P. Nuckolls, D. Wong, R. L. Lee, X. Liu, K. Watanabe, T. Taniguchi, and A. Yazdani, Evidence for unconventional superconductivity in twisted bilayer graphene, Nature (London) **600**, 240 (2021).

[28] Y. Saito, J. Ge, K. Watanabe, T. Taniguchi, and A. F. Young, Independent superconductors and correlated insulators in twisted bilayer graphene, Nat. Phys. **16**, 926 (2020).

[29] Y. Cao, J. M. Park, K. Watanabe, T. Taniguchi, and P. Jarillo-Herrero, Pauli-limit violation and re-entrant superconductivity in moiré graphene, Nature (London) **595**, 526 (2021).

[30] G. Chen, A. L. Sharpe, P. Gallagher, I. T. Rosen, E. J. Fox, L. Jiang, B. Lyu, H. Li, K. Watanabe, T. Taniguchi, J. Jung, Z. Shi, D. Goldhaber-Gordon, Y. Zhang, and F. Wang, Signatures of tunable superconductivity in a trilayer graphene moiré superlattice, Nature (London) **572**, 215 (2019).

[31] G. W. Burg, B. Lian, T. Taniguchi, K. Watanabe, B. A. Bernevig, and E. Tutuc, Evidence of emergent symmetry and valley chern number in twisted double-bilayer graphene, arXiv:2006.14000.

[32] M. Koshino, Band structure and topological properties of twisted double bilayer graphene, Phys. Rev. B **99**, 235406 (2019).

[33] A. Ghosh, S. Chakraborty, U. Ghorai, A. K. Paul, K. Watanabe, T. Taniguchi, R. Sensarma, and A. Das, Evidence of a compensated semimetal with electronic correlations at the CNP of twisted double bilayer graphene, arXiv:2211.02654.

[34] M. A. Metlitski and S. Sachdev, Quantum phase transitions of metals in two spatial dimensions. I. Ising-nematic order, Phys. Rev. B **82**, 075127 (2010).

[35] J. A. Hertz, Quantum critical phenomena, Phys. Rev. B **14**, 1165 (1976).

[36] A. J. Millis, Effect of a nonzero temperature on quantum critical points in itinerant fermion systems, Phys. Rev. B **48**, 7183 (1993).

[37] J. Lee, P. Strack, and S. Sachdev, Quantum criticality of reconstructing fermi surfaces in antiferromagnetic metals, Phys. Rev. B **87**, 045104 (2013).

[38] I. Vekhter and A. V. Chubukov, Non-Fermi-Liquid Behavior in Itinerant Antiferromagnets, Phys. Rev. Lett. **93**, 016405 (2004).

[39] T. Senthil, A. Vishwanath, L. Balents, S. Sachdev, and M. P. A. Fisher, Deconfined quantum critical points, Science **303**, 1490 (2004).

[40] J. Polchinski, Low-energy dynamics of the spinon-gauge system, Nucl. Phys. B **422**, 617 (1994).

[41] T. Senthil, M. Vojta, and S. Sachdev, Weak magnetism and non-Fermi liquids near heavy-fermion critical points, Phys. Rev. B **69**, 035111 (2004).

[42] M. A. Metlitski and S. Sachdev, Quantum phase transitions of metals in two spatial dimensions. II. Spin density wave order, Phys. Rev. B **82**, 075128 (2010).

[43] A. Fischer, Z. A. H. Goodwin, A. A. Mostofi, J. Lischner, D. M. Kennes, and L. Klebl, Unconventional superconductivity in magic-angle twisted trilayer graphene, npj Quantum Mater. **7**, 5 (2022).

[44] S. Carr, C. Li, Z. Zhu, E. Kaxiras, S. Sachdev, and A. Kruchkov, Ultraheavy and ultrarelativistic dirac quasiparticles in sandwiched graphenes, Nano Lett. **20**, 3030 (2020).

[45] Z. A. H. Goodwin, V. Vitale, X. Liang, A. A. Mostofi, and J. Lischner, Hartree theory calculations of quasiparticle properties in twisted bilayer graphene, Electron. Struct. **2**, 034001 (2020).

[46] Y. W. Choi and H. J. Choi, Strong electron-phonon coupling, electron-hole asymmetry, and nonadiabaticity in magic-angle twisted bilayer graphene, Phys. Rev. B **98**, 241412(R) (2018).

[47] S. Carr, S. Fang, Z. Zhu, and E. Kaxiras, Exact continuum model for low-energy electronic states of twisted bilayer graphene, Phys. Rev. Res. **1**, 013001 (2019).

[48] M. Christos, S. Sachdev, and M. S. Scheurer, Correlated Insulators, Semimetals, and Superconductivity in Twisted Trilayer Graphene, Phys. Rev. X **12**, 021018 (2022).

[49] X. Li, F. Wu, and A. H. MacDonald, Electronic structure of single-twist trilayer graphene arXiv:1907.12338.

[50] C. Shen, Y. Chu, Q. Wu, N. Li, S. Wang, Y. Zhao, J. Tang, J. Liu, J. Tian, K. Watanabe, T. Taniguchi, R. Yang, Z. Y. Meng, D. Shi, O. V. Yazyev, and G. Zhang, Correlated states in twisted double bilayer graphene, Nat. Phys. **16**, 520 (2020).

[51] E. McCann and M. Koshino, The electronic properties of bilayer graphene, Rep. Prog. Phys. **76**, 056503 (2013).

[52] Y. Lemonik, I. L. Aleiner, C. Toke, and V. I. Fal'ko, Spontaneous symmetry breaking and lifshitz transition in bilayer graphene, Phys. Rev. B **82**, 201408(R) (2010).

[53] A. Varlet, D. Bischoff, P. Simonet, K. Watanabe, T. Taniguchi, T. Ihn, K. Ensslin, M. Mucha-Kruczyński, and V. I. Fal'ko, Anomalous Sequence of Quantum Hall Liquids Revealing a Tunable Lifshitz Transition in Bilayer Graphene, Phys. Rev. Lett. **113**, 116602 (2014).

[54] P. Rickhaus, G. Zheng, J. L. Lado, Y. Lee, A. Kurzmann, M. Eich, R. Pisoni, C. Tong, R. Garreis, C. Gold, M. Masseroni, T. Taniguchi, K. Wantanabe, T. Ihn, and K. Ensslin, Gap opening in twisted double bilayer graphene by crystal fields, Nano Lett. **19**, 8821 (2019).

[55] F. Haddadi, Q. Wu, A. J. Kruchkov, and O. V. Yazyev, Moireé flat bands in twisted double bilayer graphene, Nano Lett. **20**, 2410 (2020).

[56] X. Liang, Z. A. H. Goodwin, V. Vitale, F. Corsetti, A. A. Mostofi, and J. Lischner, Effect of bilayer stacking on the atomic and electronic structure of twisted double bilayer graphene, Phys. Rev. B **102**, 155146 (2020).

[57] B. I. Halperin and T. M. Rice, The excitonic state at the semiconductor-semimetal transition, Solid State Phys. **21**, 115 (1968).

[58] D. Khveshchenko and H. Leal, Excitonic instability in layered degenerate semimetals, Nucl. Phys. B **687**, 323 (2004).

[59] Z. Zhang, E. C. Regan, D. Wang, W. Zhao, S. Wang, M. Sayyad, K. Yumigeta, K. Watanabe, T. Taniguchi, S. Tongay, M. Crommie, A. Zettl, M. P. Zaletel, and F. Wang, Correlated interlayer exciton insulator in heterostructures of monolayer WSe$_2$ and moiré WS$_2$/WSe$_2$, Nat. Phys. **18**, 1214 (2022).

[60] D. Chen, Z. Lian, X. Huang, Y. Su, M. Rashetnia, L. Ma, L. Yan, M. Blei, L. Xiang, T. Taniguchi, K. Watanabe, S. Tongay, D. Smirnov, Z. Wang, C. Zhang, Y.-T. Cui, and S.-F. Shi, Excitonic insulator in a heterojunction moiré superlattice, Nat. Phys. **18**, 1171 (2022).

[61] J. Eisenstein, Exciton condensation in bilayer quantum Hall systems, Annu. Rev. Condens. Matter Phys. **5**, 159 (2014).

[62] Z. Wang, D. A. Rhodes, K. Watanabe, T. Taniguchi, J. C. Hone, J. Shan, and K. F. Mak, Evidence of high-temperature exciton condensation in two-dimensional atomic double layers, Nature (London) **574**, 76 (2019).

[63] A. Kogar, M. S. Rak, S. Vig, A. A. Husain, F. Flicker, Y. I. Joe, L. Venema, G. J. MacDougall, T. C. Chiang, E. Fradkin, J. van Wezel, and P. Abbamonte, Signatures of exciton condensation in a transition metal dichalcogenide, Science **358**, 1314 (2017).

[64] J. I. A. Li, T. Taniguchi, K. Watanabe, J. Hone, and C. R. Dean, Excitonic superfluid phase in double bilayer graphene, Nat. Phys. **13**, 751 (2017).

[65] L. Ju, L. Wang, T. Cao, T. Taniguchi, K. Watanabe, S. G. Louie, F. Rana, J. Park, J. Hone, F. Wang, and P. L. McEuen, Tunable excitons in bilayer graphene, Science **358**, 907 (2017).

[66] Y. Zhang, K. Jiang, Z. Wang, and F. Zhang, Correlated insulating phases of twisted bilayer graphene at commensurate filling fractions: A Hartree-Fock study, Phys. Rev. B **102**, 035136 (2020).

[67] F. Xie, N. Regnault, D. Călugăru, B. A. Bernevig, and B. Lian, Twisted symmetric trilayer graphene. II. Projected Hartree-Fock study, Phys. Rev. B **104**, 115167 (2021).

[68] F. Guinea and N. R. Walet, Electrostatic effects, band distortions, and superconductivity in twisted graphene bilayers, Proc. Natl. Acad. Sci. **115**, 13174 (2018).

[69] C. T. S. Cheung, Z. A. H. Goodwin, V. Vitale, J. Lischner, and A. A. Mostofi, Atomistic hartree theory of twisted double bilayer graphene near the magic angle, Electron. Struct. **4**, 025001 (2022).

[70] J. Kang and O. Vafek, Strong Coupling Phases of Partially Filled Twisted Bilayer Graphene Narrow Bands, Phys. Rev. Lett. **122**, 246401 (2019).

[71] Y. Jia, P. Wang, C.-L. Chiu, Z. Song, G. Yu, B. Jäck, S. Lei, S. Klemenz, F. A. Cevallos, M. Onyszczak, N. Fishchenko, X. Liu, G. Farahi, F. Xie, Y. Xu, K. Watanabe, T. Taniguchi, B. A. Bernevig, R. J. Cava, L. M. Schoop *et al.*, Evidence for a monolayer excitonic insulator, Nat. Phys. **18**, 87 (2022).

[72] T. Cea and F. Guinea, Band structure and insulating states driven by Coulomb interaction in twisted bilayer graphene, Phys. Rev. B **102**, 045107 (2020).

[73] F. Wu, E. Hwang, and S. Das Sarma, Phonon-induced giant linear-in-t resistivity in magic angle twisted bilayer graphene: Ordinary strangeness and exotic superconductivity, Phys. Rev. B **99**, 165112 (2019).

[74] A. A. Patel and S. Sachdev, Theory of a Planckian metal, Phys. Rev. Lett. **123**, 066601 (2019).

[75] D. L. Maslov, V. I. Yudson, and A. V. Chubukov, Resistivity of a Non-Galilean–Invariant Fermi Liquid near Pomeranchuk Quantum Criticality, Phys. Rev. Lett. **106**, 106403 (2011).

[76] H. K. Pal, V. I. Yudson, and D. L. Maslov, Resistivity of non-Galilean-invariant Fermi and non-Fermi liquids, Lith. J. Phys. **52**, 142 (2012).

[77] A. Lucas and S. Sachdev, Memory matrix theory of magnetotransport in strange metals, Phys. Rev. B **91**, 195122 (2015).

[78] A. A. Patel, H. Guo, I. Esterlis, and S. Sachdev, Universal theory of strange metals from spatially random interactions, arXiv:2203.04990.

[79] S. A. Hartnoll, R. Mahajan, M. Punk, and S. Sachdev, Transport near the Ising-nematic quantum critical point of metals in two dimensions, Phys. Rev. B **89**, 155130 (2014).

[80] S. Sachdev, Quantum criticality: Competing ground states in low dimensions, Science **288**, 475 (2000).

[81] S. Sachdev, Quantum phase transitions of antiferromagnets and the cuprate superconductors, in *Modern Theories of Many-Particle Systems in Condensed Matter Physics* (Springer, Berlin, 2012), pp. 1–51.

[82] C. Liu, V. F. C. Humbert, T. M. Bretz-Sullivan, G. Wang, D. Hong, F. Wrobel, J. Zhang, J. D. Hoffman, J. E. Pearson, J. S. Jiang, C. Chang, A. Suslov, N. Mason, M. R. Norman, and A. Bhattacharya, Observation of an antiferromagnetic quantum critical point in high-purity LaNiO₃, Nat. Commun. **11**, 1402 (2020).

[83] A. Klein, A. V. Chubukov, Y. Schattner, and E. Berg, Normal State Properties of Quantum Critical Metals at Finite Temperature, Phys. Rev. X **10**, 031053 (2020).

[84] S. Chen, M. He, Y.-H. Zhang, V. Hsieh, Z. Fei, K. Watanabe, T. Taniguchi, D. H. Cobden, X. Xu, C. R. Dean, and M. Yankowitz, Electrically tunable correlated and topological states in twisted monolayer–bilayer graphene, Nat. Phys. **17**, 374 (2021).

[85] Z. A. H. Goodwin, L. Klebl, V. Vitale, X. Liang, V. Gogtay, X. van Gorp, D. M. Kennes, A. A. Mostofi, and J. Lischner, Flat bands, electron interactions, and magnetic order in magic-angle mono-trilayer graphene, Phys. Rev. Mater. **5**, 084008 (2021).